Cold Regions Science and Technology 218 (2024) 104096

Contents lists available at ScienceDirect

Cold Regions Science and Technology

journal homepage: www.elsevier.com/locate/coldregions

Design, development and deployment of a novel sea spray collector for sea-spray flux measurements

Sushmit Dhar [a,*], Masoud Naseri [a], Hassan Abbas Khawaja [b], Kåre Edvardsen [b], Tiantian Zhu [a]

[a] Department of Technology and Safety, UiT The Arctic University of Norway, Tromsø, Norway
[b] Department of Automation and Process Engineering, UiT The Arctic University of Norway, Tromsø, Norway

ARTICLE INFO

Keywords:
Sea-spray icing
Sea-spray flux measurement
Fish farm icing
Cyclone separator
Sea spray collector

ABSTRACT

The risk of sea-spray icing on vessels and marine structures in cold regions highlights the need for an accurate and robust marine-icing estimation model. To develop such a model, it is crucial to accurately determine the quantity of liquid water available for freezing on the structure, as it directly influences ice formation. As sea spray constitutes the primary source of liquid water contributing to marine icing, researchers have often focused on measuring sea-spray flux from field campaigns to establish empirical expressions for icing estimation. However, due to the lack of standardised equipment or methods for such measurements and concerns regarding the generalisability and transferability of resulting empirical expressions, researchers have resorted to employing a variety of equipment and techniques tailored to their specific research requirements. Nevertheless, these approaches have inherent limitations. This paper introduces a novel spray collector device inspired by the cyclone separator, capable of performing real-time autonomous spray flux measurements on vessels and moving platforms. The collector is constructed using carbon fibre-infused nylon material, ensuring durability in harsh cold marine climates. Computational Fluid Dynamics (CFD) simulations and laboratory tests demonstrate that the design of the new collector is more efficient than that of the previously employed devices, particularly at higher wind speeds. The device is currently deployed on a fish farm in Northern Norway in order to assess its performance in field conditions. The paper also shares preliminary findings, experiences, and limitations encountered during the deployment period.

1. Introduction

Ice accretion on ships and marine structures can significantly impact crew safety, and sea-keeping performance, impair critical machinery and systems, and may compromise structural stability leading to capsizing, as seen in the recent tragic incidents of the sinking of the fishing vessel ONEGA on 28 December 2020 (Dhar et al., 2022), and capsizing of fishing vessel Scandies Rose on 31 December 2019 (NTSB, 2020). In order to address this issue, various approaches have been employed, including establishing regulations, implementing winterization techniques, and providing marine icing forecast warnings.

International codes and standards such as IMO Polar code (IMO, 2017), ISO 19906:2019 (ISO, 2019), N-003:2017 (NORSOK Standard, 2017), LR (LR, 2023), DNV-RU-SHIP Pt.6 Ch.6 (DNV, 2023) have established guidelines to set the minimum stability criteria for vessels and marine structures operating in cold regions. These regulations consider the potential risk of icing that may be encountered and are typically based on simplified and generalised equations for icing allowances (Mintu et al., 2016), which may be an overly conservative approach as it is based on a limited number of calibration data sets focused on particular geographic regions (Mintu and Molyneux, 2022). Winterization involves implementing measures and techniques to ensure the vessel or structure can safely operate in cold weather conditions (Baller, 1983; Cho et al., 2017). These measures may include applying anti-icing or de-icing systems, which can be active methods utilising power such as heating systems, or passive methods that do not primarily rely on power such as insulating critical components or using manual tools such as hammers and shovels (DNV, 2021). However, smaller ships, particularly fishing vessels vulnerable to icing, may lack sufficient power for active methods, and during hazardous icing events, it may not be feasible for the crew to use passive techniques (Naseri and Barabady, 2016; Barabadi et al., 2016). It is also important to consider that even with the implementation of anti- and de-icing measures, it does not guarantee safety in severe conditions (Deshpande et al., 2021).

* Corresponding author.
E-mail address: sushmit.dhar@uit.no (S. Dhar).

https://doi.org/10.1016/j.coldregions.2023.104096
Received 15 October 2023; Received in revised form 12 December 2023; Accepted 13 December 2023
Available online 19 December 2023
0165-232X/© 2023 The Author(s). Published by Elsevier B.V. This is an open access article under the CC BY license (http://creativecommons.org/licenses/by/4.0/).

Hence the best approach is to avoid such situations altogether based on reliable weather warnings.

Over the past few decades, advancements in meteorology research have resulted in improved icing prediction for vessels operating in cold regions. By incorporating meteorological and oceanographic forecasts, the icing estimation models, such as the Modified Overland model (Overland et al., 1986; Overland, 1990; Desjardins, 2013), Modified Stallabrass model (Stallabrass, 1980; Henry, 1995), and the Marine-Icing Model for the Norwegian Coast Guard (MINCOG) (Samuelsen et al., 2017) evaluate the icing rate for a particular type of vessel. The output provides icing-forecast information, which is often used to issue warnings, usually in the form of icing-rate maps (e.g., Fig. 1; also see Barents Sea icing climatology (Naseri and Samuelsen, 2019)). This information can assist operators in making informed decisions regarding route planning to avoid such conditions, operation scheduling, and implementing appropriate anti-icing or de-icing measures.

In icing estimation models, ice accretion is mainly determined by the heat exchange between the surrounding environment and the liquid water flux that is available to freeze on the structure (Samuelsen, 2017; Makkonen, 1987). It is also well known from observations from vessels and marine structures that sea spray is the main source of liquid water contributing to marine icing (Zakrzewski, 1987; Jones and Andreas, 2009; Samuelsen and Graversen, 2019). According to Kulyakhtin (2014), the accuracy of the modelling of heat exchange part in the icing estimation model is relatively high given the extensive research conducted in laboratories (Panov, 1976; Foy et al., 1987; Launiainen et al., 1983; Makkonen, 1987; Stallabrass, 1980; Carstens et al., 1984; Vefsnmo, 1985; Kulyakhtin et al., 2013, 2016) and some field settings (Tabata et al., 1963; Minsk, 1984; Horjen et al., 1986; Ryerson and Longo, 1992). Thus, the primary source of uncertainty in icing estimation arises from the limited availability of spray flux measurements (Kulyakhtin, 2014).

The incoming spray flux is produced from two primary sources, one generated from the impact between waves and the hull, and the other formed by the wind tearing off droplets from wave crests, resulting in spume droplets. Various factors, including the structure shape, size, speed of the vessel, and the orientation of the hull or structure relative to waves and wind influence the incoming spray flux under specific meteorological and oceanographic conditions (Bodaghkhani et al., 2016; Dehghani et al., 2018, 2016a, 2016b). The complexities associated with the trajectory of water droplets by airflow and the unique interactions with different structures make it challenging to directly apply theoretical and observational results between vessels or structures (Roebber and Mitten, 1987). To address this challenge, researchers emphasise conducting spray flux measurements on multiple vessels and marine structures under diverse meteorological and oceanographic conditions to develop a robust spray flux model for enhancing the accuracy of marine icing estimation.

There have been some field campaigns conducted to collect spray data on vessels (Tabata, 1969; Horjen et al., 1986; Borisenkov et al., 1975; Zakrzewski and Lozowski, 1989; Ryerson and Longo, 1992; Ozeki and Sagawa, 2013; Ozeki et al., 2016a, 2018; Teigen et al., 2019), offshore structures (Jorgensen, 1986, 1985, 1984; Minsk, 1984), and even islands (Muzik and Kirby, 1992; Jones and Andreas, 2013, 2014; Andreas, 2016). Some of the data are utilised to develop empirical spray-flux formulae, which are consequently utilised as input for the icing estimation models. However, there can be differences in the output of these formulas (see table 1. in Forest et al. (2005)). Notably, the ICEMOD icing estimation model (Horjen and Vefsnmo, 1985) developed by the Norwegian Hydrotechnical Laboratory and the RIGICE04 model (Forest et al., 2005) developed by the Canadian Atmospheric Environment Service exhibit a significant disparity in spray flux input. The formula used in ICEMOD estimates 10–1000 times less spray flux than the formula used in RIGICE04 (Kulyakhtin and Tsarau, 2014). This discrepancy in spray flux may be due to the different structures considered, as ICEMOD incorporates spray generated by waves interacting with a semisubmersible (Jorgensen, 1985), while RIGICE04 measures spray after wave interaction with an island (Muzik and Kirby,

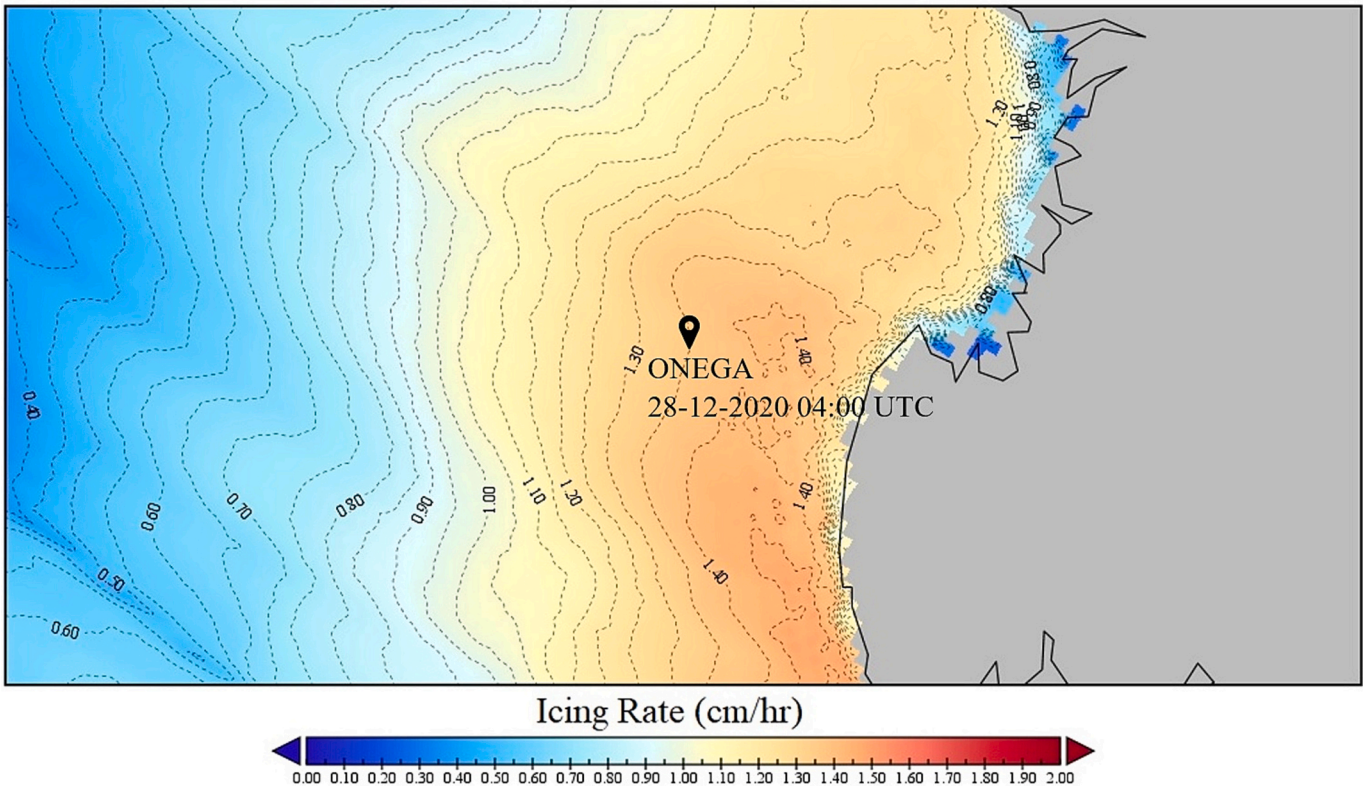

Fig. 1. Icing-rate map during ONEGA capsizing event at 28-12-2020 04:00 UTC, according to MINCOG model.

1992). Nevertheless, Kulyakhtin (2014) argues that the reported disparity cannot be solely attributed to variations in structure geometry and the reason needs further investigation. The accuracy of a model is intricately linked to the quality and comprehensiveness of the data used in its development, and this, in turn, is influenced by the accuracy of the equipment utilised for data collection.

Collecting spray data from the field in the hazardous cold marine environment, characterised by high winds, waves, and cold temperatures, poses significant challenges. This presents logistical, technological, cost, and safety obstacles (Roebber and Mitten, 1987; Dhar and Khawaja, 2021). Furthermore, there is an absence of standardised equipment and methods for spray data collection (Ryerson and Longo, 1992). Each team implemented or designed its own devices and techniques to collect field data. Various devices have been utilised for collecting spray-flux data, such as absorbent materials (Tabata, 1969; Jorgensen, 1984; Jones and Andreas, 2014), optical instruments (Andreas, 2016; Ozeki and Sagawa, 2013), and catching-type collectors (Horjen et al., 1986; Jorgensen, 1984; Muzik and Kirby, 1992; Ozeki et al., 2016a; Ryerson and Longo, 1992; Teigen et al., 2019).

Absorbent materials are cost-effective and easily deployable; however, they are susceptible to saturation requiring frequent replacements and may not be effective in locations receiving high incoming spray flux. Researchers also deployed optical instruments like Spray Particle Counter (SPC) (Ozeki et al., 2016a) and the cloud-imaging probe (CIP) (Andreas, 2016), which can count spray droplets by size as they pass through optical sensors. However, their limited droplet size measurement ranges (SPC: 100–1000 μm, CIP: 12.5 μm to 287.5 μm in diameter) do not fully capture the spectrum of sea spray droplet sizes observed in previous field measurements (0.02 μm to 7.7 mm in diameter) (Ryerson, 1995; Veron, 2015). Additionally, these devices are expensive, fragile, and may require frequent upkeep when deployed in saline marine environments. Catching-type collectors (i.e., the collectors that directly capture and collect spray droplets) are commonly preferred due to their practicality, as these do not require complex systems, are easy to construct, and suitable for prolonged deployment in challenging field conditions.

Catching-type rain gauge designs, like drums (Muzik and Kirby, 1992) and the "Cold Regions Research Engineering Laboratory" (CRREL) vertical collector (Ryerson and Longo, 1992), were used for vertical sea-spray flux measurement. However, these designs are susceptible to "wind-induced undercatch," resulting in measurement underestimation, particularly at higher wind speeds (Pollock et al., 2018). This error arises from pressure bias near the gauge orifice, deflecting spray droplets away from the inlet. Solutions may involve experimental (Cauteruccio et al., 2021) and numerical methods (Colli and Lanza, 2016), and windshields (Colli et al., 2016) or choosing a proper gauge installation location to minimise this effect (Weller et al., 2008).

Various catching-type designs have been employed for measuring horizontal spray flux, including pipe bend collectors (Jorgensen, 1986, 1985, 1984; Horjen et al., 1986) (Fig. 2 (a)), Marine rain gauge type Spray gauge (MRS) (Ozeki et al., 2016b) (Fig. 2(b)), collector plate of RigSpray Fluxmeter (Teigen et al., 2019) (Fig. 2(c)). However, insight from CFD simulations by Dhar et al. (2023) highlights a common limitation, which affects the accurate representation of spray flux measurements, especially at higher wind speeds. This limitation is associated with their bluff body designs, causing pressure bias to induce flow separation, deflecting the airstream away. As a result, smaller droplets bypass the device inlet, with only larger droplets with more body force having the potential to enter. This effect becomes more pronounced as wind speed increases, leading to reduced collection efficiency. The CRREL horizontal spray interceptor (Walsh et al., 1992) (Fig. 2(d)), features an efficient flow-through design that minimises flow separation caused by pressure perturbations (discussed in Section 2.5). Nevertheless, its efficiency also decreases with rising wind speeds, as some droplets escape prior to entering the measurement chamber, as further elaborated in Section 3.3. Accounting for this efficiency decrease can be challenging, and it can introduce errors in the empirical formulae derived from the collected data, and subsequently affect the accuracy of the icing model.

This highlights the need for a reliable spray flux measurement device that can accurately work even in strong winds, as higher wind speeds are associated with adverse weather situations that generate spray, which may lead to severe icing events in cold conditions. In addition to an efficient design for capturing sea spray, it is desirable for the device to operate without frequent human assistance and withstand harsh conditions, enabling long-term measurements, on both fixed and moving structures. Cost-effectiveness is also important to facilitate the deployment of multiple devices, allowing for a comprehensive understanding of spray distribution on marine structures.

To address these gaps, the SPRICE sea spray collector is introduced in this paper as a novel device designed for measuring horizontal sea-spray flux. The collector consists of two parts, with the first part featuring a catching-type design inspired by the cyclone separator. This innovative design allows for efficient separation and collection of air-borne sea spray droplets, isolating them from the airflow. The second part is an R. M. Young model 50,202, which is an automatic gauge for measuring the collected spray amounts in real-time. The SPRICE sea spray collector design is evaluated for airflow efficiency using Computational Fluid Dynamics (CFD) simulations. ANSYS® Fluent CFD solver is used to simulate steady-state wind flow with Reynolds-averaged Navier-Stokes (RANS) equations and the k-ω Shear Stress Transport (SST) turbulence model (Menter et al., 2003; Menter, 1994). The collector is subsequently 3D printed using carbon fibre-infused nylon material for enhanced durability in harsh marine climates. Complementing the CFD simulation

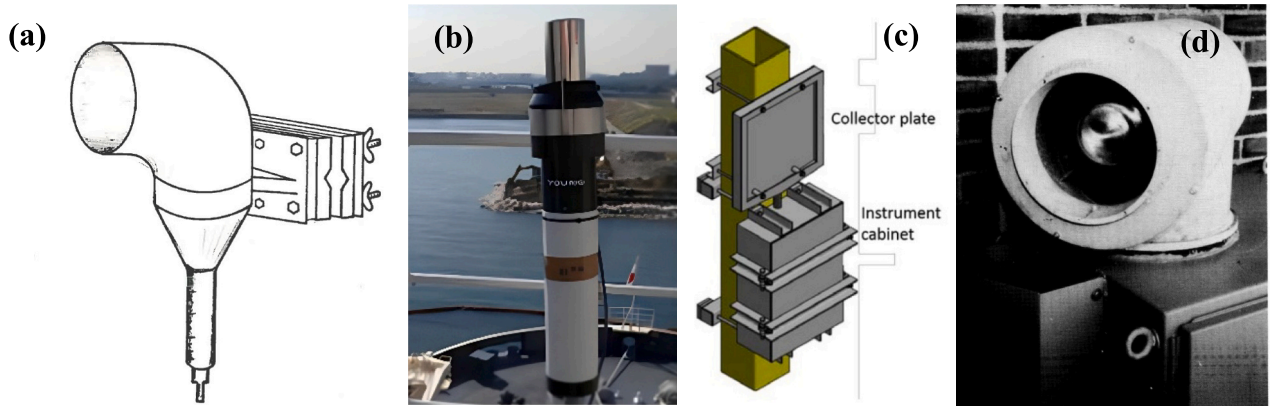

Fig. 2. Horizontal catching-type sea spray flux measurement devices (a) Pipe bend collector (Horjen et al., 1986); (b) MRS (Ozeki et al., 2016b); (c) RigSpray Fluxmeter (Teigen et al., 2019); (d) CRREL horizontal spray interceptor (Walsh et al., 1992).

results, laboratory tests are conducted to evaluate the collector's performance and asses its efficiency compared to other devices.

The collector is put to the test by deploying it at a fish farm situated in Northern Norway, where the vulnerability of fish cages to sea-spray icing and related damages is a concern. The paper also highlights the preliminary findings obtained from this field installation, shedding light on the device performance feasibility in practical marine environments. Furthermore, the study acknowledges and discusses the limitations and challenges faced during the deployment, offering valuable insights into the real-world implementation of the device.

The rest of the paper is organised as follows: Section 2 discusses the design and development of the proposed SPRICE sea spray collector; Section 3 focuses on experimental validation; Section 4 provides insights into field deployment experiences, and Section 5 presents the study's conclusion.

2. Proposed novel spray collector

2.1. SPRICE sea spray collector concept and design

According to Veron (2015), wind-generated sea spray droplets exhibit sizes varying from 0.01 μm to 6 mm in radii, while Ryerson (1995) observed droplets ranging from 14 μm to 7.7 mm in diameter resulting from wave impact with the ship's hull during the Midgett expedition (Ryerson and Longo, 1992). The smaller droplets with a low Stokes number ($<< 1$) almost instantaneously respond to airflow fluctuations due to their negligible inertia and consequently tend to closely adhere to the airstream (Jebakumar and Abraham, 2016). If the inlet of the catching-type spray collector experiences high-pressure build-up, smaller droplets may fail to enter the collector and deviate from their intended path due to flow perturbation, leading to a reduction in collection efficiency (Dhar et al., 2023). Therefore, it is crucial for an efficient spray collector to maintain a balanced inflow and outflow of air to prevent pressure build-up at the inlet. Moreover, once the spray droplets enter the collector, it is essential to intercept and separate them from the airflow to prevent their escape with the outflow. The effective capture of smaller droplets ensures the successful collection of larger droplets as well, as larger droplets possess greater body force making them less influenced by surrounding airflow change, thereby, more likely to enter the collector. These serve as the fundamental principles behind designing an efficient spray collector for capturing sea spray droplets and measuring accurate sea-spray flux.

The SPRICE sea spray collector is developed by incorporating these principles in order to address the challenges associated with measuring sea spray flux. The design of the collector draws conceptual inspiration from the cyclone separator (Fig. 3.), which is a mechanical device commonly employed in industrial processes for particle separation entrained in a fluid stream (gas or liquid) (Hoffmann and Stein, 2008).

The cyclone separators consist of a cylindrical chamber with a tangential inlet for fluid with entrained particles, a top outlet for cleaned fluid, and a bottom outlet for separated particles. The balanced orbital theory (Barth, 1956; Dietz, 1981) is the widely adopted theory explaining particle separation based on opposing forces within the separator (Hoffmann and Stein, 2010; Song et al., 2016). The fluid carrying the particles enters through the tangential inlet and spirals downward as the outer vortex, with centrifugal force pushing particles towards the wall. An inner vortex forms closer to the centre, moving upward, which causes inward drag force, pushing particles inward. The inward drag is directly proportional to the particle diameter, while the outward centrifugal force is proportional to the diameter cube (Hoffmann and Stein, 2010). Hence, larger particles dominated by centrifugal force, spiral down to the bottom for collection, while smaller particles with less inertia may escape through the top exhaust.

The SPRICE sea spray collector (Fig. 4.) is designed to effectively capture and separate sea spray droplets from the airflow while ensuring a balanced inflow and outflow to avoid pressure build-up at the inlet. It

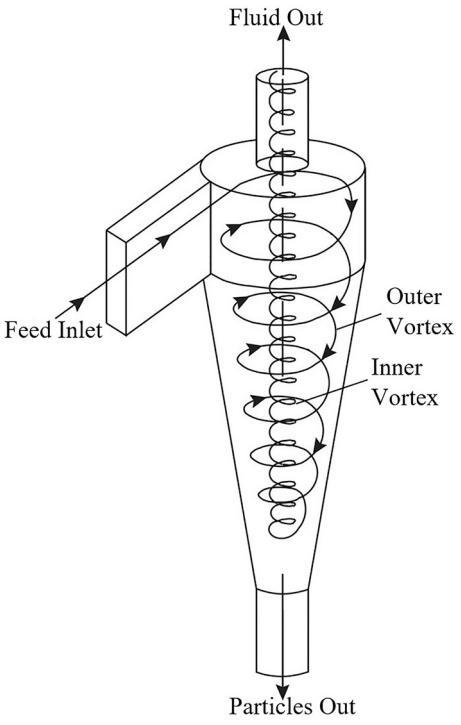

Fig. 3. Schematic diagram of a conical reverse-flow cyclone separator illustrating the fundamental operating principle (Hoffmann and Stein, 2008).

incorporates design features, including a large exhaust, provision for air outlet from the bottom, and an absence of constriction inside, which promote unobstructed airflow. The round inlet minimises directional bias, while its truncated conical shape widening inward leverages the Venturi effect (Venturi, 1797) to reduce pressure perturbations. The involute feed directs the airflow slightly downward into the cylindrical body, where the separation of droplets from the airflow occurs. The upper part of the cylinder extends to a flat annular surface with a 0.5 cm high concentric rim, designed to contain upward swirling droplets and block them from escaping through the exhaust. The U-shaped exhaust primarily allows air to escape while preventing vertical precipitation from entering the device. The lower part of the cylinder tapers to an inner funnel-shaped section that channels the separated droplets to the spray amount measuring device. Fig. 5 depicts the final design of the SPRICE collector, with its dimensions achieved through iterative optimisation following CFD simulations (see Sections 2.3 and 2.4) to attain the desired airflow outcome.

2.2. Spray measurement device

During previous field expeditions, the measurement of collected spray amounts from catching-type devices such as pipe bend collectors (Fig. 2 (a)) (Horjen et al., 1986) and drums (Muzik and Kirby, 1992) involved visual readings. However, conducting manual measurements can be challenging, particularly during stormy conditions, due to safety concerns and device inaccessibility, which may limit data collection and introduce human error. Subsequently, researchers transitioned to automated measurement devices in the later field campaigns. The Midgett expedition (Ryerson and Longo, 1992) used the capacitive wired measurement system developed by CRREL, which enabled automatic logging of the spray amount at regular intervals. However, the device exhibited high noise levels in the reading, likely due to the presence of saltwater. The RigSpray fluxmeter (Teigen et al., 2019) is designed with a tipping bucket and pressure gauge for autonomous spray level measurement. Tipping buckets are usually not employed on unsteady platforms due to potential measurement errors induced by

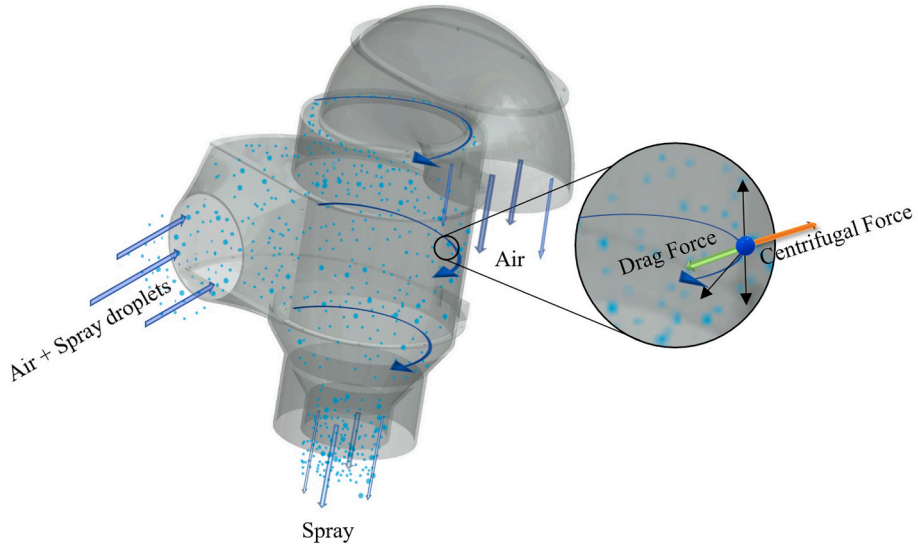

Fig. 4. Working principle of the SPRICE sea spray collector.

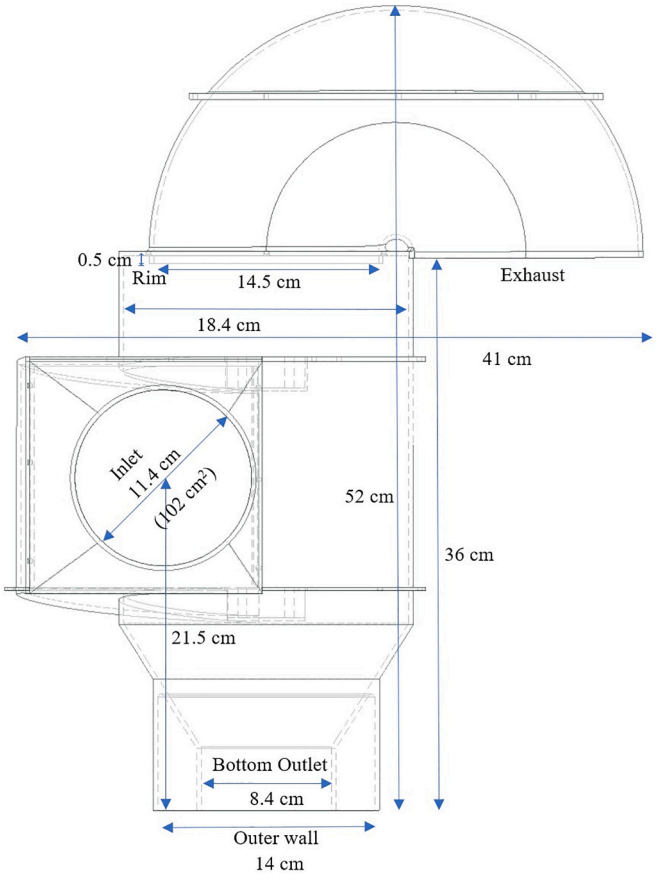

Fig. 5. Schematic of the SPRICE sea spray collector.

motion. Ryerson and Longo (1992) also noted this issue and rejected the use of tipping buckets for the Midgett expedition. The R. M. Young automatic precipitation gauge model 50,202 was utilised both during the Midgett expedition (Ryerson and Longo, 1992) as well as in the MRS (Ozeki et al., 2016b). Unlike the capacitive measuring system used in the Midgett expedition, this device did not exhibit notable noise with saline water. Additionally, no notable issues were reported during its use with the MRS (Ozeki, personal communication, 2022).

For the SPRICE sea spray collector, the R. M. Young automatic precipitation gauge model 50,202 (Fig. 6.) is chosen for measuring the collected spray amount based on promising results from previous field expeditions (Ryerson and Longo, 1992; Ozeki, personal communication, 2022). This gauge is specifically manufactured to work effectively on moving platforms like ships and buoys (Cole et al., 2011; Weller et al., 2008). According to its specifications, the gauge has good corrosion resistance, ensuring its longevity, and it comes with a heater, making it usable in a wide temperature range (−20 °C to +50 °C). When the gauge becomes full, a self-siphon process drains the measuring tube in approximately 30 s, during which measurements cannot be taken. Although during this process, error may be introduced (Serra et al., 2001), it is unlikely to be a significant concern as long as the incoming spray flux is not substantial during that period. The catchment part of this gauge fits between the gap at the bottom of the SPRICE collector's

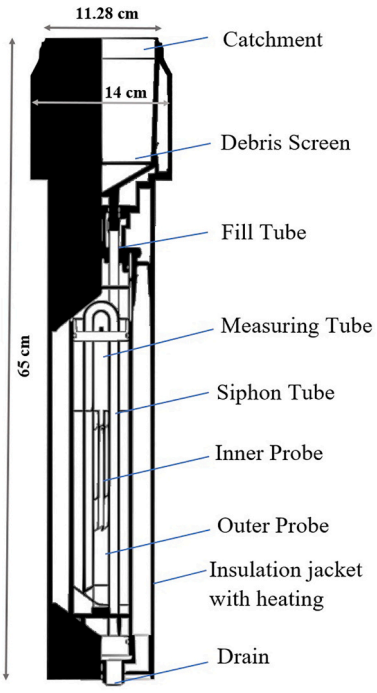

Fig. 6. R. M. Young automatic precipitation gauge model 50202.

bottom outlet and the outer wall. The bottom outlet feeds the collected spray into the gauge, while the outer wall acts as a barrier, preventing spray from entering the device from the bottom.

2.3. SPRICE collector design evaluation through CFD simulations

In this study, steady-state airflow is simulated using the RANS equations and the k-ω SST turbulence model (Appendix A.). These simulations allow for the evaluation of velocity and pressure distribution fields, providing insight into the behaviour of airborne spray droplets with low Stokes numbers inside and around the collector. The simulation results are used to optimise the design of the SPRICE collector, ensuring that it facilitates proper inflow and outflow while minimising pressure build-up at the inlet. To evaluate the qualitative performance of the collector, the time-averaged wind velocity and pressure information from the RANS simulations is deemed sufficient as it provides a basis for comparison against alternative designs, including those used in past expeditions. The focus was not on capturing a precise snapshot of the parameters at a specific instant using computationally intensive models, but rather on understanding the collector's overall behaviour and performance. The CFD simulations were conducted with initial wind velocities of 5, 15, and 30 m/s. These three values were selected to represent the most probable levels of wind speeds that are expected in field scenarios. The upper level, 30 m/s, corresponds to a violent storm scenario (Beaufort scale 11), the mid-level, 15 m/s, corresponds to a near gale scenario (Beaufort scale 7), and the lower level, 5 m/s, corresponds to a moderate breeze scenario (Beaufort scale 3). Studying the behaviour of the device under these varying velocities provides a comprehensive understanding of its flow characteristics in different field conditions. For illustrative purposes, Figs. 7 and 8 present the 15 m/s scenario.

The CFD simulation results demonstrate that as the airflow enters the circular orifice and progresses through the truncated conical inlet into a larger internal chamber, it experiences a decrease in pressure at the inlet (Fig. 7 (a)) due to the Venturi effect (Venturi, 1797). This pressure reduction induces a suction effect, facilitating the inflow of air (Fig. 7 (b)) with minimal velocity reduction.

The air is then guided through the involute feed, which promotes laminar flow and minimises turbulence by distributing the airflow evenly (Ji et al., 2019). When the air is fed into the cylindrical body, it is forced into a spiral motion, and an outer vortex is formed, travelling downward. When the air reaches the bottom, an inner vortex of a smaller diameter is formed, reverses direction, and spirals upward, exiting through the exhaust pipe (Fig. 8). Also, the pressure near the wall is higher and gradually decreases as one moves towards the centre in the radial direction, becoming negative to maintain equilibrium in the rotating flow pattern (Hoffmann and Stein, 2010). The simulation results exhibit the effectiveness of the SPRICE collector's design in achieving balanced airflow, preventing significant pressure build-up at the inlet, thus minimising flow separation.

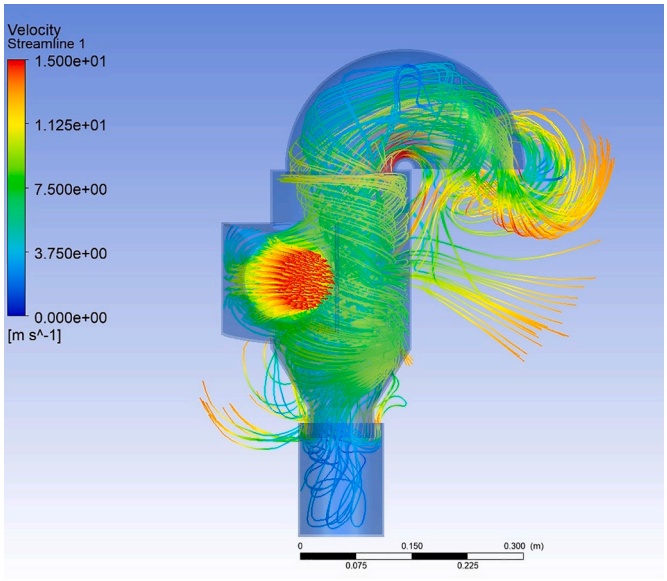

Fig. 8. The CFD simulation (at 15 m/s) showing airflow pattern inside the SPRICE spray collector.

2.4. SPRICE and CRREL collector comparison through CFD

Dhar et al. (2023) conducted an extensive critical review of the spray flux measuring devices utilised in prior field expeditions and used CFD simulations to analyse their performance. Their results demonstrate that the CRREL horizontal spray interceptor (Walsh et al., 1992) outperforms other catching-type collector designs in terms of airflow. In the CRREL design, the airborne spray droplets enter through a constricted inlet into an internal chamber double its diameter (Fig. 9). The droplets then flow around a convex baffle, with larger droplets falling into the measuring

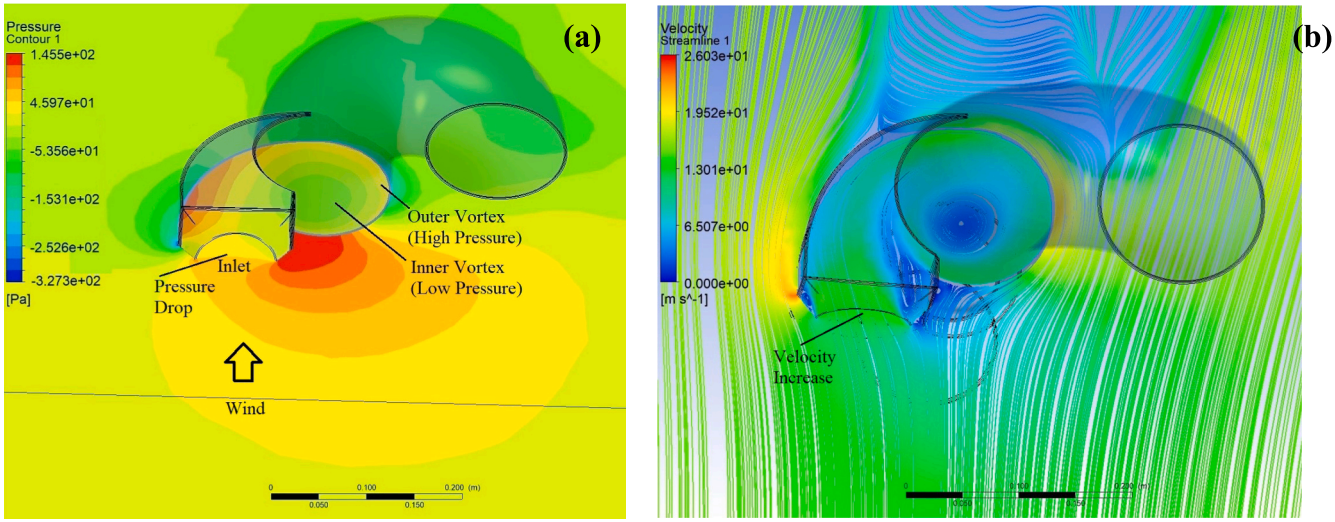

Fig. 7. The CFD simulation (at 15 m/s) (a) depicts the pressure field (with gauge pressure shown) across the inlet of the SPRICE spray collector; (b) showing airflow streams.

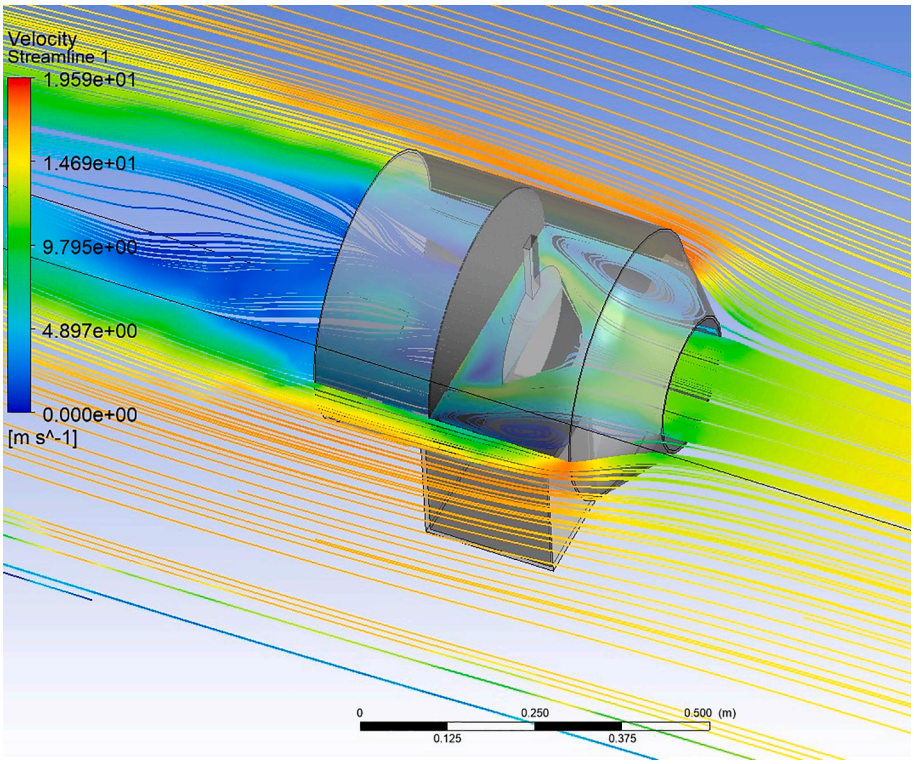

Fig. 9. CFD simulation (at 15 m/s) showing the wind flow around the CRREL horizontal spray interceptor (Dhar et al., 2023).

tank, while smaller droplets carried by the wind are intercepted by a mesh at the back and gradually trickle down into the measuring tank. This flow-through configuration is efficiently designed to minimise pressure build-up at the inlet, causing minimal flow separation and maximising the airflow for accurate spray collection.

Given its notable performance, the CRREL design was used as the benchmark to assess the airflow efficiency of the SPRICE collector. CFD simulations were performed (keeping consistent parameters) to compare the airflow performance of the SPRICE spray collector with that of the CRREL design. The analysis focused on evaluating the pressure build-up at the inlet and the resulting drop in wind velocity due to flow stream separation. Average wind velocity and pressure were computed at the inlet plane for both devices, considering initial simulated wind velocities of 5, 15, and 30 m/s. The velocity streamlines on the inlet plane are illustrated in Figs. 10 (a) and 10 (b) for the 15 m/s scenario. The comparison presented in Table 1 demonstrates nearly similar airflow results between the CRREL and final SPRICE collector design. While the intended airflow performance of the SPRICE collector was achieved through specific design modifications and dimension adjustments, achieving greater efficiency in SPRICE spray flux measurement than the CRREL design requires effective mitigation of the observed limitations in their design, which is further discussed in Section 3.3.

2.5. SPRICE collector fabrication and mounting

The SPRICE spray collector is fabricated using an industrial carbon

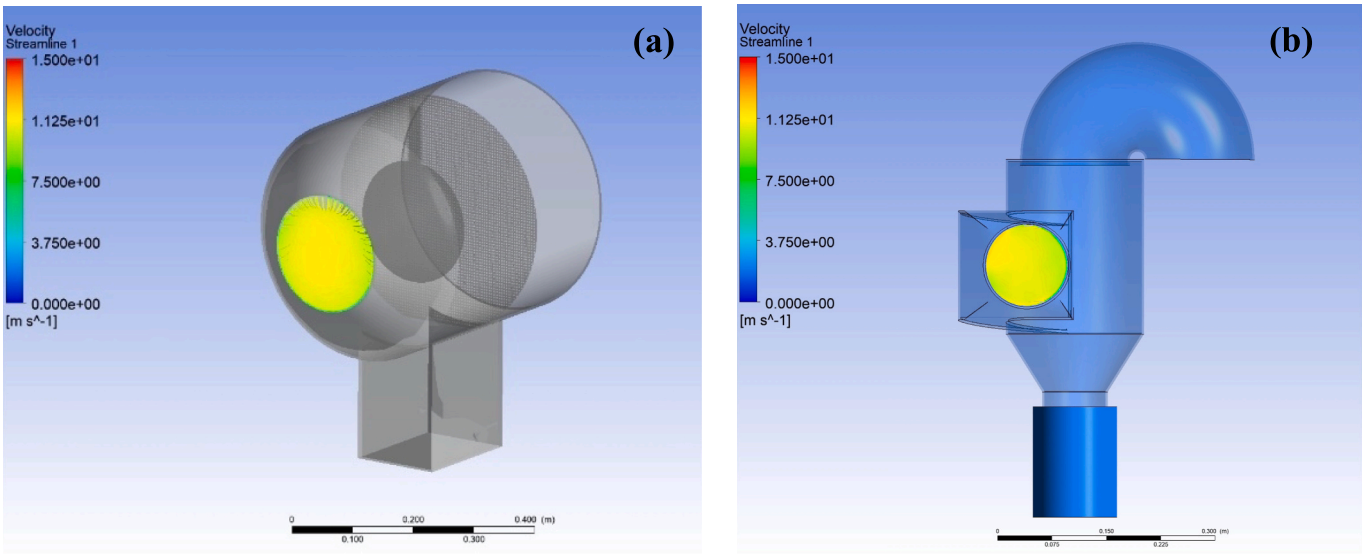

Fig. 10. Velocity streamline (15 m/s simulation) at the inlet plane of (a) CRREL-designed horizontal spray interceptor and (b) SPRICE spray collector.

Table 1
Simulation comparison between CRREL design and SPRICE design spray collector.

Parameters	CRREL design			SPRICE design		
Initial simulated wind velocity (m/s)	5	15	30	5	15	30
Average wind velocity at the inlet plane (m/s)	3.6	10.7	21.8	3.6	10.7	21.1
Velocity reduction at the inlet plane (m/s)	1.4	4.3	8.2	1.4	4.3	8.9
Ratio of inlet wind velocity and initial wind velocity	3.6/5 = 0.72	10.7/15 = 0.71	21.8/30 = 0.72	3.6/5 = 0.72	10.7/15 = 0.71	21.1/30 = 0.70
Average gauge pressure* at the inlet plane (Pa)	10.0	79.3	318.3	8.4	74.4	323.1

* Gauge pressure refers to the pressure measured relative to the atmospheric pressure.

fibre 3D printer (Markforged, 2023). The use of 3D printing technology simplifies the manufacturing process and enables greater design flexibility while ensuring high precision. The printing material chosen is Onyx Nylon filament with carbon fibre reinforcements due to its high strength-to-weight ratio makes the equipment both lightweight and durable. Its high stiffness and modulus of elasticity allow it to resist bending and deformation effectively. The material is highly resistant to corrosion and humidity, even in saline marine environments. Additionally, it has a low coefficient of thermal expansion, ensuring it remains unaffected by temperature changes.

The collector is printed in multiple parts and then attached together using marine grade A4 stainless steel screws (Fig. 11). Spikes are installed around the top to deter birds, as they are known to damage equipment deployed in marine environments. A white coat of marine-grade paint is applied to the surface to ensure water resistance.

Subsequently, the collector and the R.M. Young 50202 are both mounted on a stainless-steel pipe (Fig. 12). The collector is positioned on top of the catchment part of the gauge, ensuring proper alignment between the bottom outlet of the collector and the outer wall while maintaining a gap. This configuration allows for unobstructed airflow and prevents constriction.

Fig. 11. The 3D printed SPRICE spray collector.

Fig. 12. SPRICE spray collector mounted on top of R. M. Young automatic precipitation gauge (model 50202).

2.6. Data logging and sea-spray flux calculation

The R.M. Young 50202 gauge used in the SPRICE spray collector incorporates a measuring tube section (Fig. 6) that has a maximum capacity of 500 ml between siphon events. The spray amount is measured in terms of voltage output, which is calibrated to represent the volume of spray collected. Additionally, a data logger is required to store the measurement at regular intervals.

The data loggers utilised in this study are listed in Table 2 in Section 4.2. The loggers are installed within a weatherproof housing, ensuring protection from environmental elements. Data logging takes place at 1-min intervals, and the collected data are transmitted remotely via 4G telemetry for real-time monitoring.

The sea-spray flux $R_w\left(\mathrm{g/m^2 s}\right)$, which represents the rate at which the spray is collected and measured by the SPRICE collector, is calculated as follows:

$$R_w = \frac{V\rho_{sw} \times 1000}{At} \tag{1}$$

where $V\ \left(\mathrm{m^3}\right)$ is the spray volume measured by the R.M. Young 50202, $\rho_{sw}\ \left(\mathrm{kg/m^3}\right)$ is the sea-water density, A $\left(\mathrm{m^2}\right)$ is the inlet area of the SPRICE spray collector, which is 0.0102 $\mathrm{m^2}$, and $t\ (\mathrm{s})$ is the measurement time period.

3. Experimental validation through lab testing

In the following part, an attempt has been made to assess the efficiency of the SPRICE sea spray collector through physical experiments. Section 3.1 evaluates the airflow performance of the collector, while the subsequent section focuses on assessing the device's collection efficiency, which is the efficiency of measuring sea-spray flux. The collection efficiency is based on both the inlet efficiency, reflecting how much spray enters through the device's inlet, and the retention efficiency, indicating how much spray is retained and reaches the device's spray measuring unit. The SPRICE collector's inlet and retention efficiency are

Table 2
Instruments deployed in the field.

Instrument	Parameters measured	Location	Data logging	Notes	Reference
SPRICE sea spray collector facing WSW	Horizontal sea-spray flux	Fish Cage No.3, Collector inlet: 1.2 m above water level	1 min interval	Spray volume measured with-R. M. Young 50202 Data Transmission - 4G Telemetry, NexSens X2 Environmental Data Logger	R. M. Young Company (2023) NexSens Technology, Inc. (2023)
SPRICE sea spray collector facing ENE	Horizontal sea-spray flux	Fish Cage No.1, Collector inlet: 1.2 m above water level	1 min interval	Spray volume measured with - R. M. Young 50202 Data Transmission - 4G Telemetry, Campbell Scientific CR350 data logger	R. M. Young Company (2023) Campbell Scientific, Inc. (2023a)
OBS-Buoy400 Wave Buoy	Wave parameters and sea surface temperature	68.7° N, 17.2° E	30 min interval	Data Transmission - 4G Telemetry	Obscape BV (2023)
WS600-UMB Smart Weather Sensor	Precipitation intensity and type (Doppler radar), 2-D wind direction and speed (Ultrasonic), Temperature, relative humidity, air pressure	Barge Top, Sensor: 22 m above water level	1 min interval	Data Transmission - 4G Telemetry, Campbell Scientific CR1000X data logger	OTT HydroMet (2023) Campbell Scientific, Inc. (2023b)
SPRICE sea spray collector facing WSW	Horizontal rain flux	Barge Top, Collector inlet: 21 m above water level	1 min interval	Spray volume measured with-R. M. Young 50202 Data Transmission - 4G Telemetry, Campbell Scientific CR1000X data logger	R. M. Young Company (2023) Campbell Scientific, Inc. (2023b)
Thies Ultrasonic Anemometer 3-D	Wind velocity in X/Y/Z-direction, Acoustic-virtual temperature (Ultrasonic)	Barge Top, Sensor: 22 m above water level	1 s interval	Data Transmission - 4G Telemetry, Campbell Scientific CR800 data logger	Adolf Thies GmbH and Co KG (2023) Campbell Scientific, Inc. (2023c)

evaluated in Section 3.2 under controlled laboratory conditions. In Section 3.3, the retention efficiency of the SPRICE collector is compared to the CRREL horizontal spray interceptor (Ryerson and Longo, 1992).

3.1. SPRICE collector airflow performance

The SPRICE collector's airflow performance was tested in a laboratory setting (Fig. 13), where air blowers were used to create turbulent wind speeds of up to 15 m/s at the location of the collector inlet, in accordance with the expected average wind speeds in field conditions during spray generation events. The objective was to analyse air velocity at the inlet and the corresponding velocity reduction from the free-flow condition due to pressure perturbations. The reduction value provides a measure of the collector's airflow efficiency. This assessment method is used to replicate the approach used for computing airflow efficiency through CFD simulations (Section 2.4).

To achieve this, a hot wire anemometer was used to measure the wind velocity at the inlet of the collector over a minute (Fig. 14 (a)). Subsequently, the collector was removed from that location, and the wind velocity in the unobstructed environment was recorded for the same duration. This process was repeated ten times. Based on the collected dataset, the average ratio of the velocity at the collector's inlet to the wind velocity in free-flow conditions was estimated 0.65, as illustrated in Fig. 14 (b). The measured ratio approximately aligns with the earlier simulation outcomes, which indicated a ratio of 0.715 (Table 1).

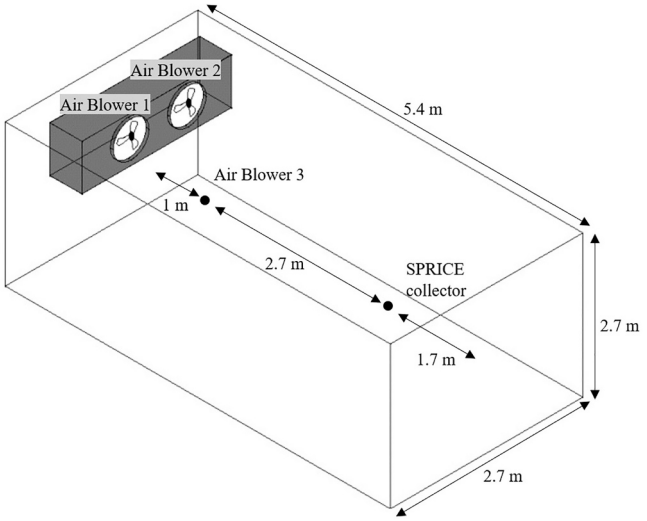

Fig. 13. Laboratory chamber dimension and air blower set up.

3.2. SPRICE collector laboratory test

Evaluating the overall collection efficiency of the SPRICE collector to measure spray flux, which includes both the inlet and retention efficiency, in real field conditions presents challenges. Determining the inlet efficiency is particularly intricate as it is difficult to ascertain the collector's ability to capture sea spray droplets of various sizes and trajectories under varying turbulent environmental conditions. Despite optimising its design to minimise pressure perturbation at the inlet, there is a possibility that some droplets may not enter the collector due to flow separation. Measuring the actual spray flux is challenging because it is hard to quantify the amount of spray that should reach the inlet of the collector without any pressure perturbation. This complexity makes calculating efficiency intricate due to the absence of a definitive reference for comparison with measurement results. Additionally, the absence of standardised equipment for relative analysis further complicates the assessment (Dhar et al., 2023; Ryerson and Longo, 1992). Consequently, an approach combining experimental testing within a controlled environment with a theoretical framework is proposed to estimate the SPRICE collector's collection efficiency.

The collection efficiency of the SPRICE collector e (%) is expressed as:

$$e = \frac{M_{experimental}}{M_{theoretical}} \times 100 \quad (2)$$

where, $M_{experimental}$ (g) is the actual mass of spray collected with the SPRICE spray collector, and $M_{theoretical}$ (g) is the theoretical mass of spray that reached the inlet area of the collector.

The experiment depicted in Figs. 15 (a) and (b) involved positioning

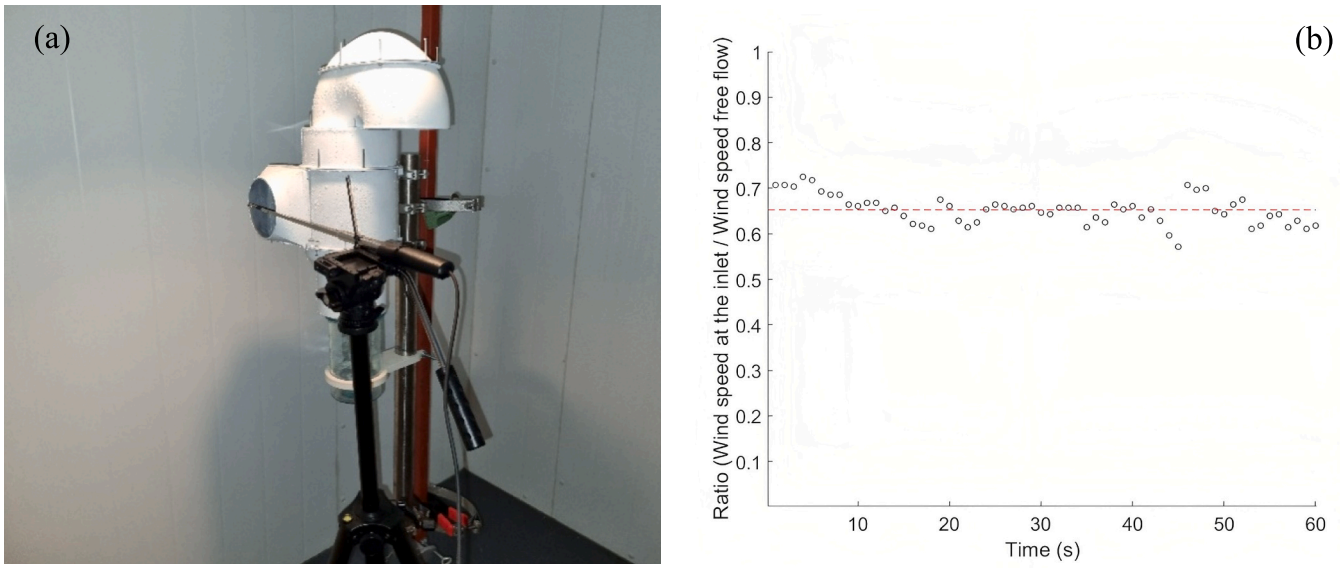

Fig. 14. (a) Wind speed measurement at the inlet of the SPRICE collector with hot wire anemometer; (b) the ratio of the wind speed at the collector's inlet compared to the measured free-flow wind speed (each data point shown in the plot is the average of the 10 repeated measurements).

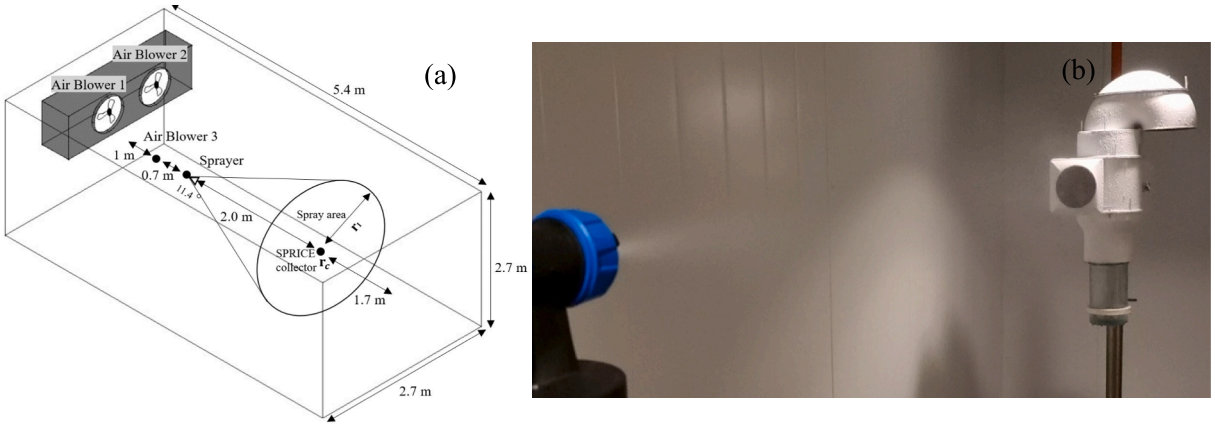

Fig. 15. (a) Laboratory arrangement during the spray test of the SPRICE collector; (b) Depicts the spray test being conducted.

a water sprayer at a distance of 2 m from the collector, aligning its spray axis towards the centre of the collector inlet. Placing the sprayer at a 2 m distance was based on the observation that, within this range, the trajectory of the spray consistently aligned with the collector inlet. Inside the test chamber, air blowers were utilised to generate wind speeds of up to 15 m/s at the collector's inlet location. The water sprayer operated at a constant flow rate of 400 ml/min (≈ 6.66 g/s) fitted with a 1.8 mm needle nozzle, producing a full cone spray pattern. The nozzle's average spray cone angle measured 11.4° (Fig. 16 (a)) and generated droplets ranging in diameter from 10 μm to 150 μm (Fig. 16 (b)), which were determined from samples captured using a high-speed camera. Over a duration of 17 m and 15 s, a total of 6900 g of water was sprayed across the entire area of radius r_1 (Fig. 15 (a)). The spray that entered through the SPRICE collector inlet of radius r_c (Fig. 15 (a)) and was subsequently collected at its bottom amounted to 480 g (i.e., $M_{experimental}$) during this period.

As the sprayed area is larger than the SPRICE collector inlet area (Fig. 15), the determination of collection efficiency by directly

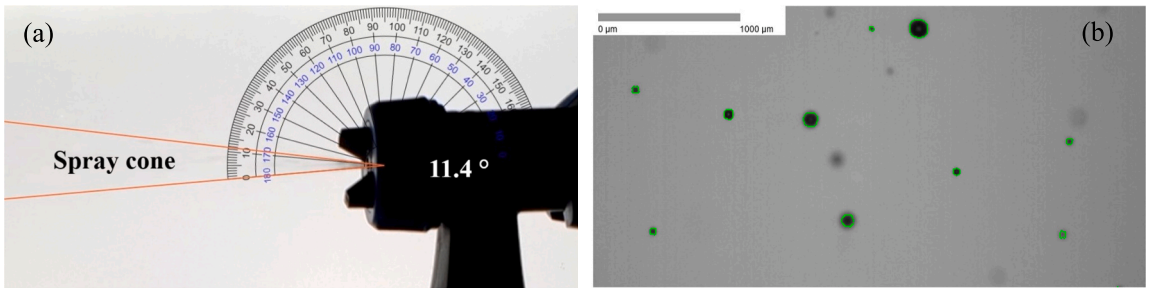

Fig. 16. (a) Showing the average spray cone angle; (b) Spray droplet image captured with the high-speed camera.

comparing the amount of water sprayed with the amount of spray collected by the collector is not applicable. Consequently, $M_{theoretical}$ is introduced to express the spray amount that reaches only the collector inlet.

In order to estimate $M_{theoretical}$ a mathematical model is proposed for the full cone spray pattern, which can be expressed as:

$$M_{theoretical} = F_{r_c}\, T \tag{3}$$

where F_{r_c} (g/s) signifies the theoretical flow rate of the spray at the inlet area of the SPRICE collector of radius $r_c = 5.7$ cm and T(s) is the total duration of spray during the experiment.

However, it is essential to recognise that the spray flux may vary across the sprayed area, and its distribution depends on the spray pattern, which in turn relies on the characteristics of the sprayer and the nozzle being used. As illustrated in Fig. 17 (a), the full cone spray pattern employed in this study initially exhibits a near-triangular distribution and gradually transforms towards a trapezoidal to near-uniform distribution as the spray emanates from the nozzle. In this experimental setup, water was sprayed from a distance of 2 m, indicating a trend towards a more uniform distribution. Nonetheless, to comprehensively assess the collection efficiency range of the SPRICE collector (e) in this study, it is assumed the spray distribution may range from triangular to trapezoidal and eventually to uniform, encompassing the spectrum of possibilities.

The spray flow rate across an area can be conceptualized as its projected volume, with its height represents the flux at each discrete point, as illustrated in Fig. 17 (b.iii). Here, r_1 denotes the radius of the circular spray area (A_{r_1}), and the flow rate at A_{r_1} signifies the volume, F_{r_1}. Additionally, r_2 is used to denote the radius of the upper base of the spray flux distribution, with h indicating its spray flux value in g/m^2/s. During the experiment, the spray cone angle of 11.4° at a 2 m distance produces a total circular spray area (A_{r_1}) of radius of $r_1 = 19.96$ cm (shown in Fig. 15 (a)). As the distribution of spray flux transitions from triangular to trapezoidal to uniform distribution, r_2 changes from $r_2 = 0$ to $r_2 = r_1$, resulting in four possible cases for F_{r_c}:

Case 1. If $r_2 = 0$, it signifies a triangular spray flux distribution (Fig. 18 (a)), then F_{r_c} can be expressed as:

$$F_{r_c} = \frac{\pi}{3} h \left(\frac{r_c^3}{r_1}\right) + \pi r_c^2 h \left(\frac{r_1 - r_c}{r_1}\right) \tag{4}$$

Case 2. If $0 < r_2 < r_c$, it signifies a trapezoidal spray flux distribution (Fig. 18 (b)), then F_{r_c} can be expressed as:

$$F_{r_c} = \frac{\pi}{3} h \left(\frac{r_c - r_2}{r_1 - r_2}\right)\left(r_2^2 + r_2.r_c + r_c^2\right) + \pi r_c^2 h \left(\frac{r_1 - r_c}{r_1 - r_2}\right) \tag{5}$$

Case 3. If $r_c \le r_2 < r_1$, it signifies a trapezoidal spray flux distribution (Fig. 18 (c)), then F_{r_c} can be expressed as:

$$F_{r_c} = h\, \pi r_c^2 \tag{6}$$

Case 4. If $r_2 = r_1$, it signifies a uniform spray flux distribution (Fig. 18 (d)), and F_{r_c} can be expressed as:

$$F_{r_c} = h\, \pi r_c^2 \tag{7}$$

By denoting the total spray flow rate by F_{r_1}, the expression for h corresponding to each of the four cases can be derived as follow:

$$h_i = \begin{cases} \dfrac{3\,F_{r_1}}{(\pi r_1^2)} \text{ Case 1 : if } r_2 = 0 \\ \dfrac{3\,F_{r_1}}{(\pi(r_1^2 + r_1.r_2 + r_2^2))} \text{ Case 2 : if } 0 < r_2 < r_c \\ \dfrac{3\,F_{r_1}}{(\pi(r_1^2 + r_1.r_2 + r_2^2))} \text{ Case 3 : if } r_c \le r_2 < r_1 \\ \dfrac{F_{r_1}}{(\pi r_1^2)} \text{ Case 4 : if } r_2 = r_1 \end{cases}, i = 1, \ldots 4 \tag{8}$$

By substituting Eq. (8) into Eqs. ((4)–(7)), and subsequently inserting the corresponding F_{r_c} expression into Eq. (3), $M_{theoretical}$ can be expressed as follows:

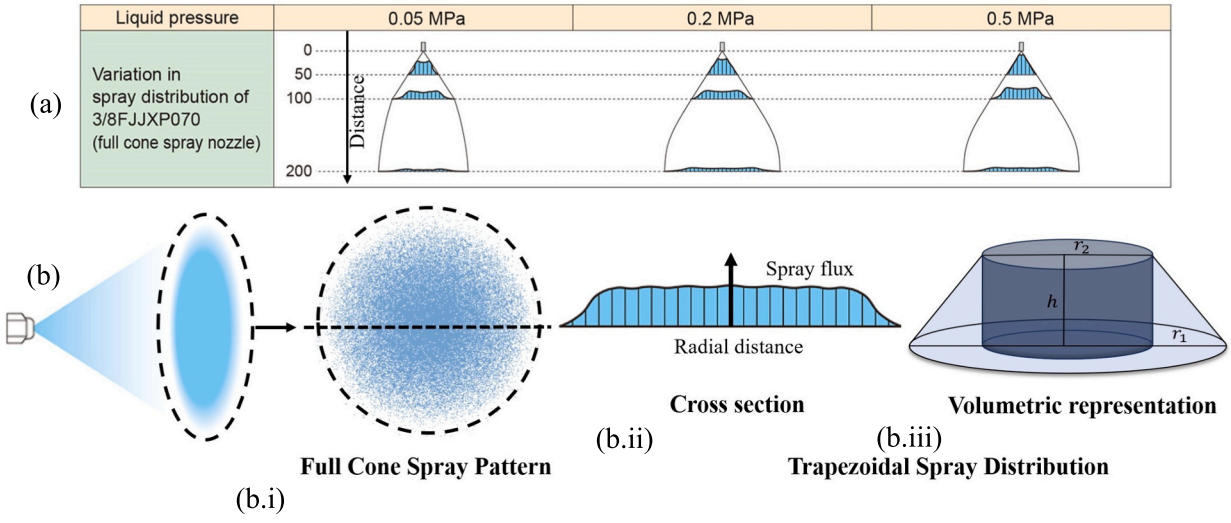

Fig. 17. (a) Variation in spray distribution with progress for a full cone spray pattern (H.IKEUCHI, and Co.,Ltd., 2023). (b.i) Full Cone spray pattern on a circular area; (b.ii) Cross Section of the spray flow with a trapezoidal distribution; (b.iii) Volumetric representation of the flow rate of the trapezoidal spray flux distribution.

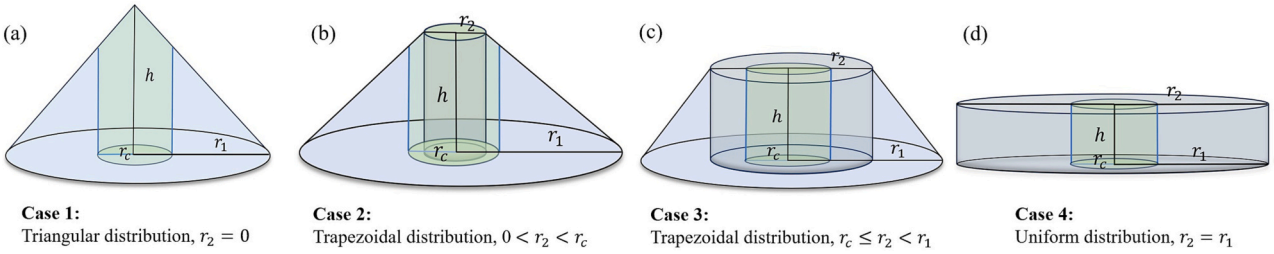

Fig. 18. The volumetric representations of F_{r_1} and F_{r_c} for (a) Case 1; (b) Case 2; (c) Case 3; (d) Case 4. F_{r_1} corresponds to the total volume shaded in blue, and F_{r_c} represents the volume swept by the collector inlet and is shaded in green. (For interpretation of the references to colour in this figure legend, the reader is referred to the web version of this article.)

$$M_{theoretical_i} = \begin{cases} \dfrac{r_c^2(3r_1 - 2r_c)}{r_1^3} F_{r_1} T \text{ Case 1 : if } r_2 = 0 \\ \left(\dfrac{3r_1 r_c^2 - 2r_c^3 - r_2^3}{(r_1^3 - r_2^3)}\right) F_{r_1} T \text{ Case 2 : if } 0 < r_2 < r_c \\ \dfrac{3r_c^2}{(r_1^2 + r_1.r_{2+}r_2^2)} F_{r_1} T \text{ Case 3 : if } r_c \leq r_2 < r_1 \\ \dfrac{r_c^2}{r_1^2} F_{r_1} T \text{ Case 4 : if } r_2 = r_1 \end{cases}, i = 1, \ldots 4 \quad (9)$$

In the experimental setup, the spray flow rate was set at 6.66 g/s. Accounting for factors such as gravity-induced droplet settling, or potential evaporation may be required. Consequently, assuming that 99.7% (equivalent to three standard deviations of a standard normal distribution) of the spray amount reaches A_{r_1} the resulting value for F_{r_1} is calculated as $F_{r_1} = 6.46$ g/s. Given $r_1 = 19.96$ cm, $r_c = 5.7$ cm and $T = 1035$ s (17 m 15 s), the $M_{theoretical}$ becomes only a function r_2 whose range can be calculated from Eq. (9) for Cases 1–4.

Subsequently, the collection efficiency (e) of the SPRICE collector during this experiment is estimated using Eq. (2), taking into account the actual spray mass collected ($M_{experimental}$), which was measured to be 480 g. The resulting values are presented in Fig. 19 for a range of spray distribution scenarios, including triangular, trapezoidal, and uniform distributions. The plot shows that the collector efficiency, e is 36% for a triangularly distributed flow rate, ranging from >36% to <86% for trapezoidal distribution and reaching 86% for a uniformly distributed spray flow rate.

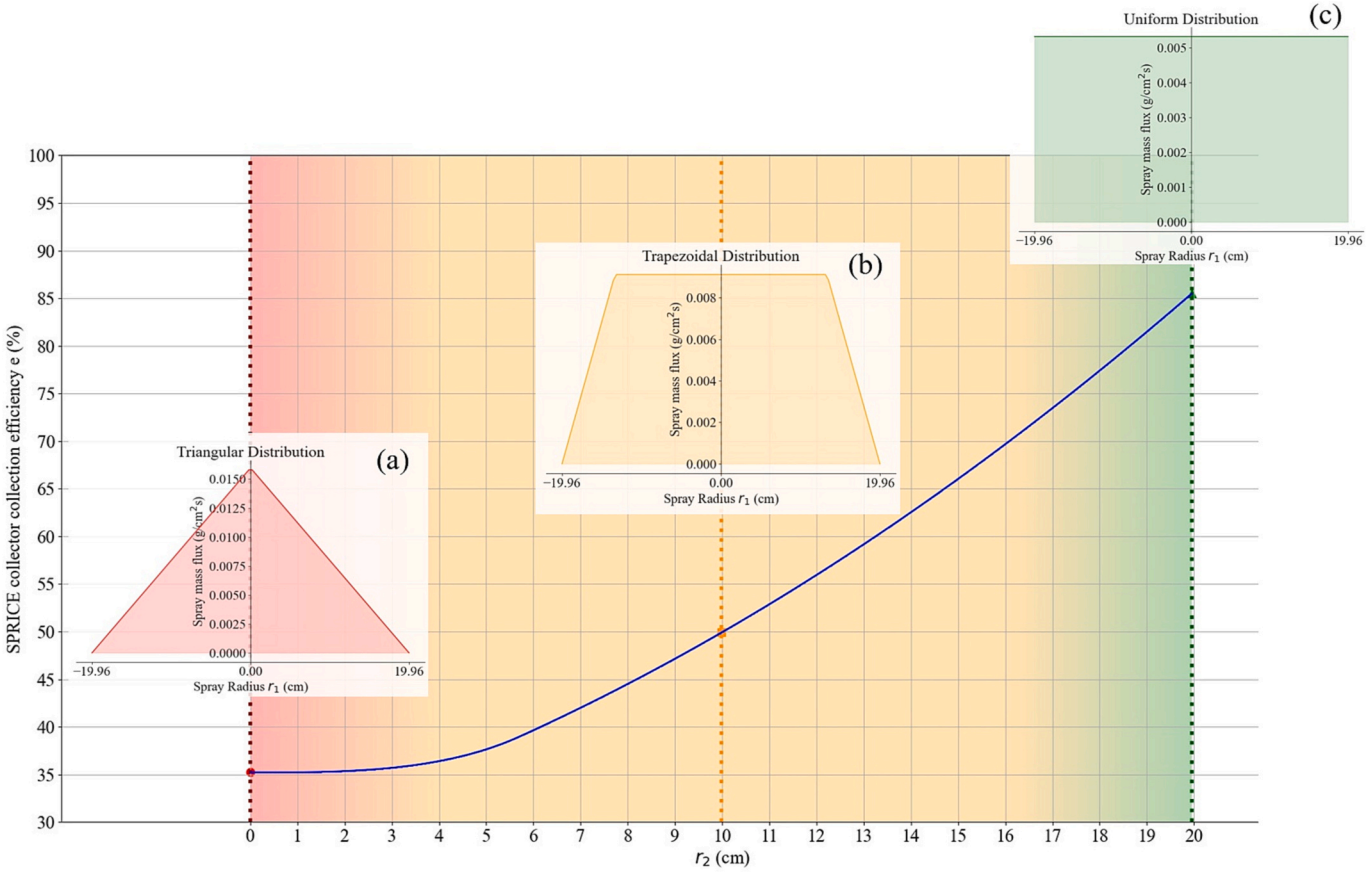

Fig. 19. SPRICE collector's collection efficiency (e) as a function of radius r_2, where subplot (a) illustrates triangular flow rate distribution when $r_2 = 0$; (b) illustrates trapezoidal flow rate distribution (here for illustration purposes, $r_2 = r_1/2$); (c) illustrates uniform flow rate distribution when $r_2 = r_1$. The background colour gradient from red fading to orange and fading to green signifies the gradual shift in the flow rate distribution, transitioning from triangular $r_2 = 0$ (i.e., Case 1) progressing to trapezoidal $0 < r_2 < r_1$ (i.e., Cases 2 and 3), and ultimately reaching uniform distribution $r_2 = r_1$ (i.e., Case 4). (For interpretation of the references to colour in this figure legend, the reader is referred to the web version of this article.)

Though the significance of the method presented here to estimate the collection efficiency of the SPRICE collector lies within a controlled laboratory environment under specific conditions, it also holds relevance for understanding its physical performance in real-field scenarios. While the experiment predominantly examined smaller droplets within the 10–150 μm range, field conditions may encompass a broader spectrum of droplet sizes (Mintu et al., 2019). During the USCGC Midgett expedition (Ryerson and Longo, 1992), the overall mean geometric median of spray droplet diameter was measured to be 234 μm (Ryerson, 1995), indicating the collector's efficiency will be relatively higher in such conditions.

Some functionalities of the collector were also visually assessed during the experiment. It was observed that as the spray droplets entered through the collector inlet, they were directed towards the outer walls of the cylindrical body. A liquid film was formed upon colliding with the wall and undergoing coalescence (Fig. 20), gradually spiralling downwards towards the bottom. Additionally, some liquid film resulting from droplet impact ascended along the wall due to the upward draft towards the roof, creating an upward swirling liquid film (USLF). The collector's concentric rim acted as a barrier, minimising USLF from flowing over the edge (i.e., lip leakage) and escaping the collector. Only a minimal amount of spray was observed to escape through the exhaust, and a small quantity of droplets remained adhered to the collector body, not reaching the bottom measuring unit.

3.3. SPRICE and CRREL collector comparison

Despite demonstrating favourable airflow performance, which indicates a high inlet efficiency, the CRREL horizontal spray interceptor (Ryerson and Longo, 1992) presents a constraint in retention efficiency, thereby impacting its overall collection efficiency. As spray enters through the inlet, some smaller droplets do not fall into the measurement tank upon encountering the baffle plate. These smaller droplets, carried by the airflow, may escape through the mesh at the back (Fig. 21 (a)). This becomes more pronounced with an increase in wind speed, resulting in a continuous decrease in retention efficiency. Walsh et al. (1992) attempted to address the issue of decreasing collection efficiency by presenting a calibration curve (Fig. 21 (b)) based on experimental results using a garden sprayer producing droplets 0.5 mm in diameter. They sprayed water into the inlet of the device, which was mounted on a pickup truck travelling at a fixed speed. The efficiency in the calibration curve was determined by calculating the mass ratio of water sprayed to the amount of water collected. This procedure was repeated at different speeds travelled by the truck, generating various wind speeds. However, this calibration curve exclusively addresses retention efficiency and does not account for inlet efficiency, as smaller droplets may fail to enter due to pressure perturbations at the collector inlet when sprayed from a distance. Additionally, the curve only considers the escape of spray droplets with a diameter of 500 μm. In reality, sea spray droplets in the field can be smaller, leading to a further decrease in retention efficiency.

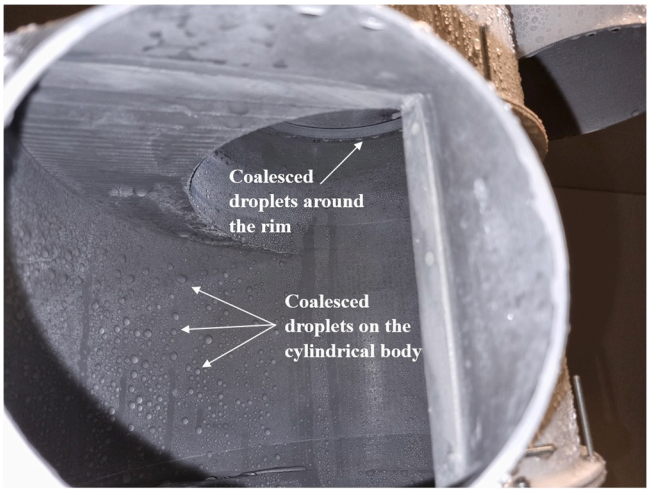

Fig. 20. View of inside the collector showing the coalescence of water droplets.

In order to compare the retention efficiency of the SPRICE collector with the CRREL device, a test was conducted to replicate the experiment performed by Walsh et al. (1992) in developing the CRREL collector efficiency curve (Fig. 21 (b)). Turbulent wind conditions were generated at approximately 30 m/s at the collector inlet within the laboratory using the blowers (shown in the experimental arrangement illustrated in Fig. 22 (a)). This approach served as an alternative to the method employed by Walsh et al. (1992), which involved using a moving pickup truck. The choice was made to test at a wind speed of 30 m/s, as this corresponds to the highest wind speed anticipated in the field. According to the efficiency graph (Fig. 21 (b)), the CRREL collector is expected to collect around 50% of the initial sprayed amount at the inlet at a wind speed of 30 m/s when the plot curve (Fig. 21 (b)) is extrapolated to 108 km/h (30 m/s).

During the SPRICE collector test, the sprayer (producing 10–150 μm droplets) was directed towards the collector inlet as depicted in Fig. 22 (b), following a setup similar to the CRREL device (Walsh et al., 1992). A total of 1600 g of water was sprayed into the inlet, and the total collected water at the bottom of the collector was weighed to be 1585 g. This represented approximately 99% of the initial volume of water sprayed, in contrast to the projected 50% by the CRREL device at this wind speed. The 1% loss can be attributed to the spray that escaped through the collector exhaust after entering or remained adhered to the collector body. The experimental results obtained at a wind speed of 30 m/s addresses the worst-case scenario, as it is expected that the escape of droplets from the SPRICE collector would be lesser at lower wind speeds. Based on this, it can be reasonably concluded that the SPRICE collector exhibits higher retention efficiency than the CRREL collector under higher wind speeds.

The comparison presented between the SPRICE collector and the CRREL device is exclusively based on retention efficiency. A definitive overall collection efficiency assessment necessitates a side-by-side comparison test under identical conditions. However, the absence of physical access to the CRREL device or availability of similar experimental test results, as conducted for the SPRICE collector in Section 3.2, prevented a direct comparison. Though it may be argued that if the inlet efficiency for both devices is similar, as indicated by comparable airflow performance in Table 1 (Section 2.4), then in that case, it can be inferred that the SPRICE collector's overall collection efficiency exceeds that of the CRREL device at higher wind speeds. This inference, however, needs to acknowledge the limitations associated with CFD simulations in replicating real-world scenarios.

4. Field deployment

The SPRICE sea spray collector is specifically designed with the intention to conduct real-time autonomous sea-spray flux measurements on both ships and other marine structures. In order to perform feasibility studies, the collector is deployed on a fish farm (Fig. 23) in Northern Norway. The primary objective is to evaluate its performance in actual field conditions and document the challenges encountered in such operational settings.

4.1. Motivation for spray flux measurement on fish farm

Fish farming in Norway typically takes place in fjords and along the coastal regions. The farms are usually made up of large, floating structures called "cages" or "pens" that are anchored to the seafloor. These cages or pens contain the fish and are designed to provide a controlled environment for them to grow. With favourable conditions for fish growth and increasing demand for seafood, the fish farming industry in

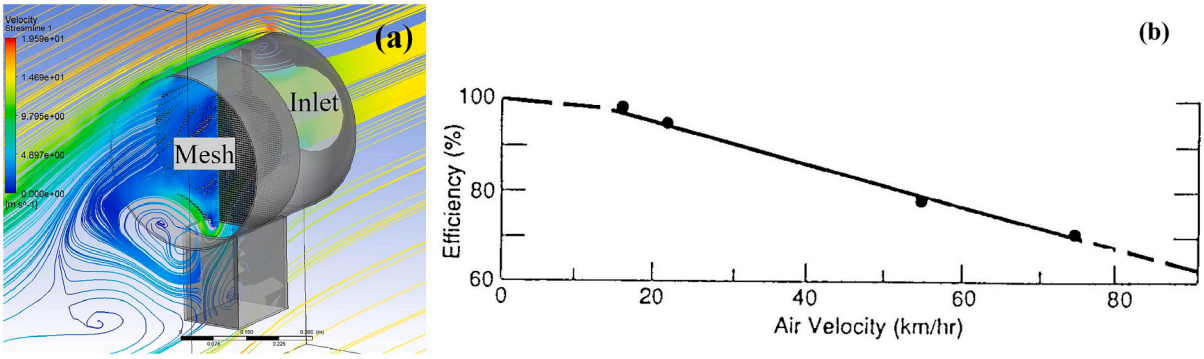

Fig. 21. (a) The CFD simulation (15 m/s) showing the wind flow from the mesh screen of the CRREL horizontal spray interceptor (Dhar et al., 2023). (b) Efficiency curve for calibration of the horizontal spray interceptor (Walsh et al., 1992).

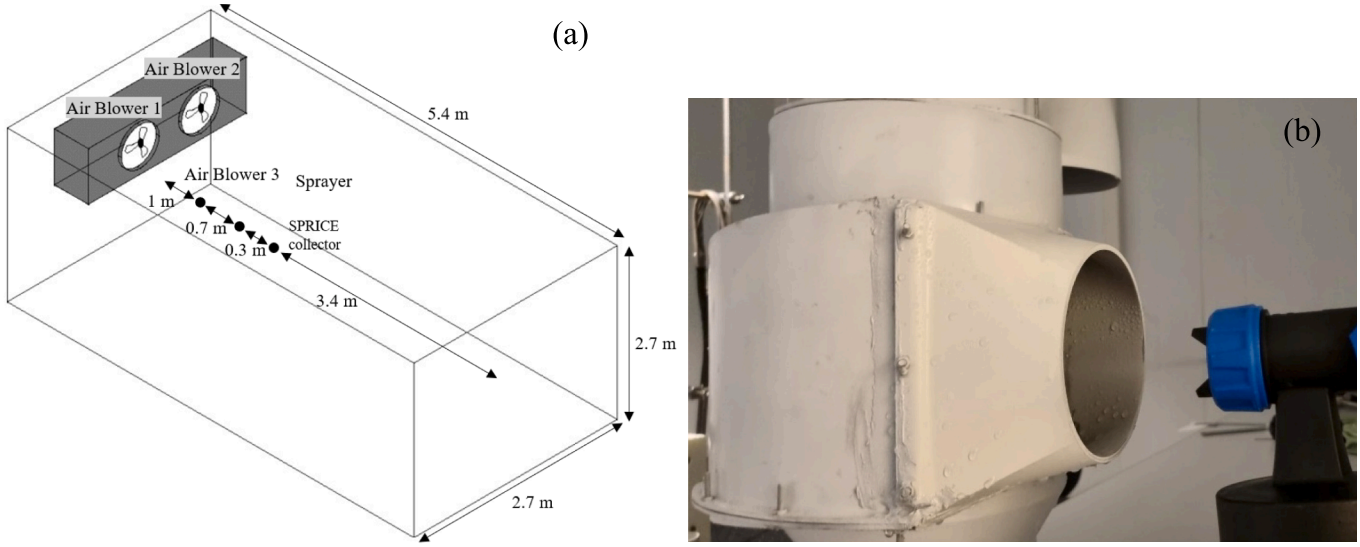

Fig. 22. (a) Experimental setup to measure the amount of spray that escapes after entering the collector at high wind speed; (b) Showing the sprayer directing spray into the SPRICE collector inlet.

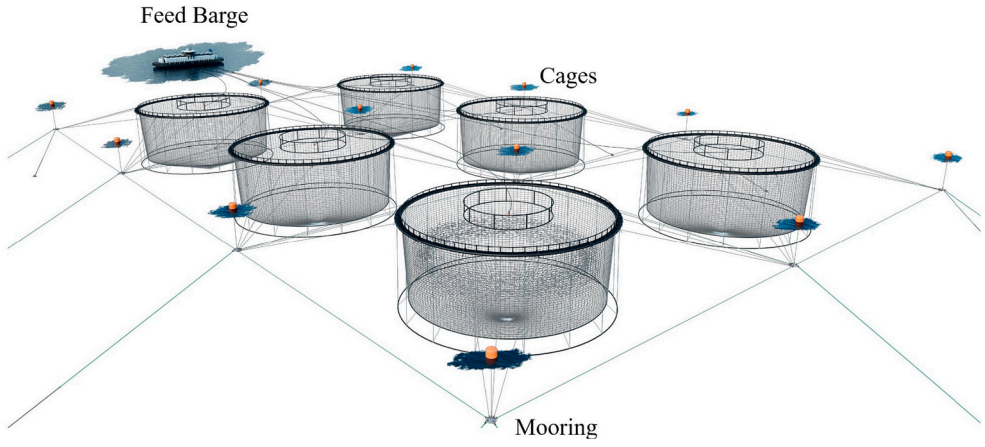

Fig. 23. Representation of a typical Norwegian fish farm setup featuring a 2 × 3 fish cage configuration (AKVA Group, 2023).

Northern Norway has experienced significant development (Bergheim, 2012). However, they are particularly vulnerable to challenges such as icing due to the cold temperatures and harsh weather conditions in the region (Jensen, 2006). The high winds, waves, heavy snowfall, and freezing temperatures can cause significant ice build-up on the cages, which can potentially cause the structure to rupture or collapse (Fig. 24). This may lead to the escape of farmed fish into the wild, which can have substantial negative impacts on the environment and local ecosystems (Marsden, 2021). Hence an accurate icing prediction model for such structures can be beneficial for the operators to take preventative actions.

As discussed, it is challenging to apply theoretical and observational

Fig. 24. Damage in a fish cage due to ice accretion in Northern Norway (Picture: Alexander Boiko).

results from one vessel or structure to another when it comes to sea spray measurements, particularly due to the complex interaction between the structure and its surrounding environment generating sea spray. Hence a spray-flux model built for vessels or offshore platforms may not provide an accurate result for fish farms. Additionally, the mountainous regions of Northern Norway is associated with complex wind flow, such as gap winds, trapped lee waves, and downslope windstorms, which can also contribute to spray generation (Dhar et al., 2022; Doyle and Shapiro, 2000). To develop accurate sea-spray flux models for fish farms in Northern Norway, it is essential to gather field data that takes into account the unique conditions of the region.

4.2. Equipment installation

The SPRICE sea spray collector is deployed on a fish farm located at Skjærvika (68.73° N, 17.23° E) in Astafjorden (Fig. 25). The site experiences prevailing strong winds and waves from the south-westerly and westerly directions and is also susceptible to potential ice accretion when strong cold winds from the North bring freezing temperatures. The fish farm comprises 12 fish cages of model Akva Polarcirkel 400 and 500 (AKVA Group, 2023). Two collectors are installed in fish farm cages to measure sea-spray flux, with one oriented to face west-southwest (WSW, bearing ~247.5°) to capture sea spray generated by the dominant winds and waves and another facing east-northeast (ENE, bearing ~067.5°) to capture the sea spray generated from the northerly winds and waves contributing to icing.

Alongside the spray flux measuring equipment, a weather station has been installed on a stable structure on the feed barge. This weather station measures additional meteorological parameters, such as wind parameters, to complement the sea-spray flux measurement. The locations of the instruments in the field are shown in Fig. 26. The feed barge is located approximately 200 m away from the fish cages. The wind measuring instrument is mounted on top of the barge, around 22 m above water level, located where the impact of local effects caused by the barge structure is minimum. Additionally, a wave buoy has been deployed in the fjord next to the cages to measure wave parameters at a water depth of around 160 m. The buoy is strategically placed away from the middle of the fjord to prevent collisions with vessel traffic, and an AIS transponder is fitted to notify the nearby vessels.

The positioning of instruments had to be carefully planned to ensure they did not interfere with the day-to-day work of the fish farm workers. The attachment of instruments to the cages and barge required custom

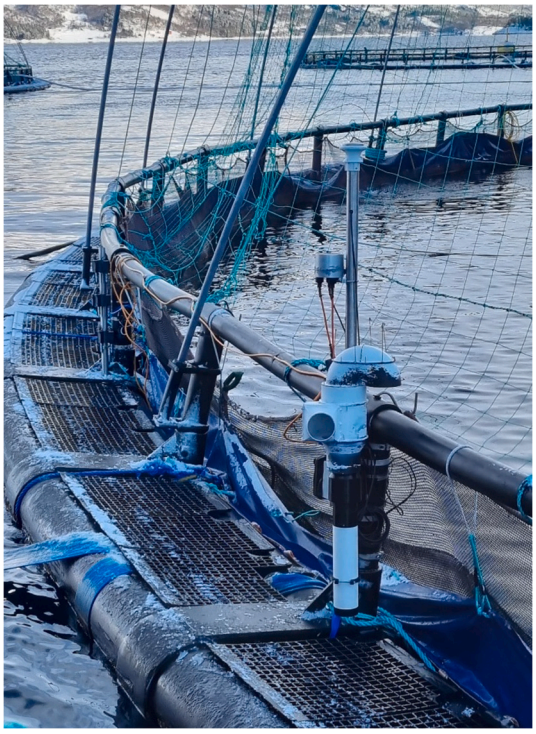

Fig. 25. SPRICE sea spray collector installed in the field.

fabrication and regular checks to ensure stability, particularly after rough weather events. The instruments on the cage are powered by the feed barge electric generator, as installing independent battery pack is cumbersome and has safety concerns with seawater contact. However, interruptions in the electricity supply are common, particularly during rough weather events when sea spray is generated. Also, the cage instruments, like the dataloggers, being close to the water level, are exposed to high humidity and may necessitate frequent replacement of desiccants (humidity absorbents) to avoid damage.

Another challenge emerged following the deployment of the collectors on the fish cage, as instances of strong winds and waves generating spray frequently occurred in conjunction with precipitation from the south-westerly and westerly directions. This made it difficult to distinguish the amount of spray and precipitation collected by the WSW SPRICE collector. To address this issue, an identical third SPRICE collector (shown in Fig. 27) was installed on top of the barge, at a height of 21 m above water level where there is usually no spray effect. The collector on the barge also faces the WSW direction, aligning with the orientation of the WSW cage collector, allowing for the collection of only horizontal rain flux from that direction. Assuming the rain contribution is the same for both on top of the barge and on the cage, the rain measurement from the barge collector can be subtracted from the measurements collected by the WSW collector on the cage to account only for the sea-spray flux.

The installation of all instruments was completed on 7 March 2023, and the collected data is being stored in the repository of the Norwegian Meteorological Institute and will be made publicly available. A summary of the instruments deployed in the field is provided in Table 2.

4.3. Preliminary data collection

An example of preliminary data collected from the SPRICE sea spray collector, during an event on 11 June 2023, between 14:15 and 15:45 UTC, is presented to demonstrate the collector's functionality and the results obtained. The significant wave height measurements ranged from 0.55 m to 0.76 m, while the average wind speed varied between 12

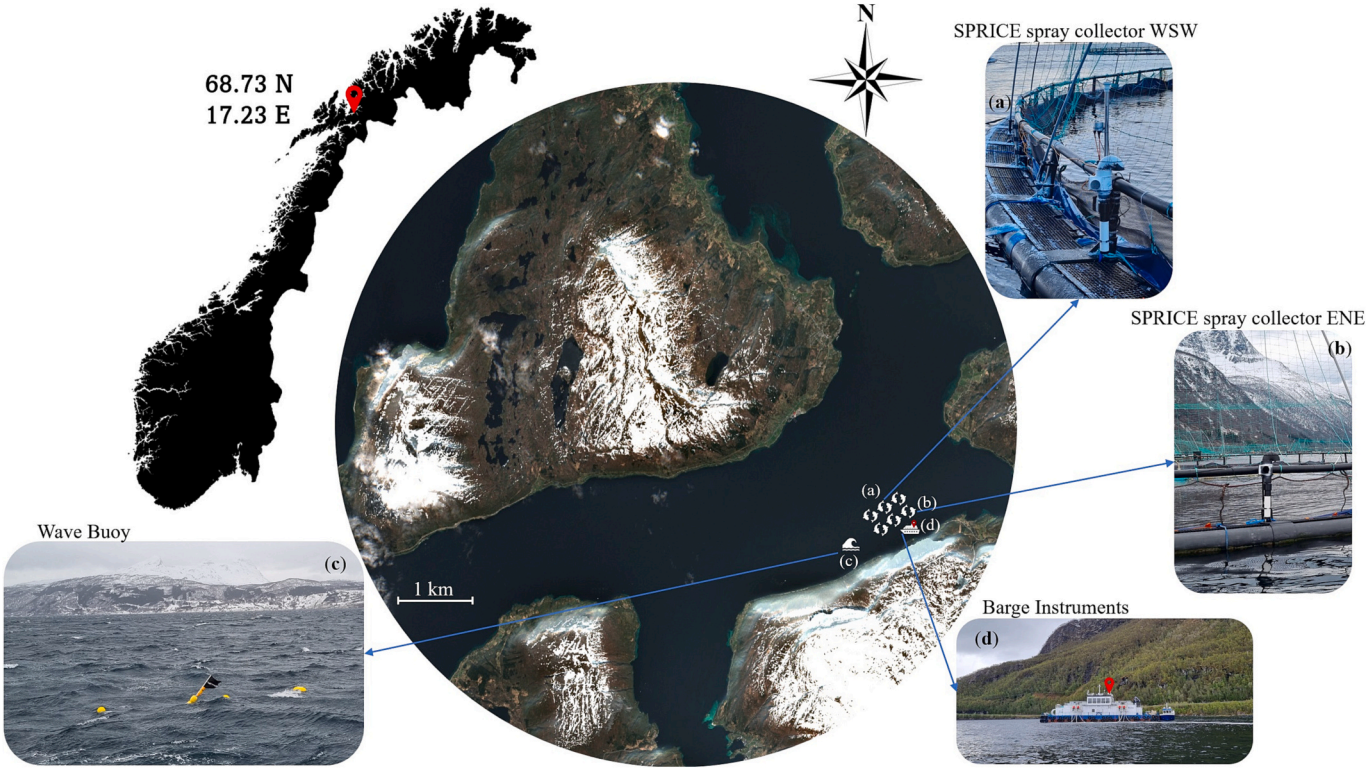

Fig. 26. Instruments deployed at Skjærvika fish farm (a) SPRICE spray collector facing WSW direction; (b) SPRICE spray collector facing ENE direction; (c) OBS-Buoy400 Wave Buoy; (d) Instruments deployed on top of the feed barge.

Fig. 27. SPRICE collector installed on top of the feed barge, facing the west-southwest (WSW) direction.

and 17 m/s. Sea-spray flux calculations are performed for one-minute intervals, utilising Eq. (1), employing an average seawater density of 1027 kg/m^3 obtained from local salinity measurements, and an average rainwater density of 1000 kg/m^3. Additionally, calculations are conducted for 30-min intervals to coincide with the wave buoy readings during the periods from the 15th to the 45th minute and then from the 45th to the 15th minute of the hour. Fig. 28 presents the data from the SPRICE collectors and the calculated sea-spray flux alongside relevant met ocean data.

In Fig. 28, graph (a) depicts the time series of spray flux measurements, where the green data points correspond to the spray collected every minute in the west-southwest direction. The data points were derived by subtracting the estimated rain contribution, which is represented by magenta data points and obtained from the SPRICE collector installed on the barge top, from the readings of the SPRICE collector located on the cage facing west-southwest, depicted by blue data points. Graph (b) shows the calculated sea-spray flux, where the right axis, featuring grey data points, represents the spray flux calculated for each minute, while the left axis, marked with green data, illustrates the spray flux calculated over a 30-min period. The data reveals that the SPRICE collector captures sea spray when the significant wave height (H_s) exceeds the 0.6 m threshold, as demonstrated by the red data points in graph (c) on the left axis. Subsequently, an increase in spray flux correlates with a rise in significant wave height in the presence of strong wind speeds, as indicated by the orange data points in graph (c) on the right axis, while the wind and wave direction, as shown in graph (d), align approximately towards the WSW collector.

4.4. Limitations of the SPRICE sea spray collector

During the deployment period, certain limitations have been identified in relation to the SPRICE sea spray collector. Firstly, its fixed attachment to the fish cage structure prevents it from rotating and aligning with changes in wind and wave directions and may lead to less

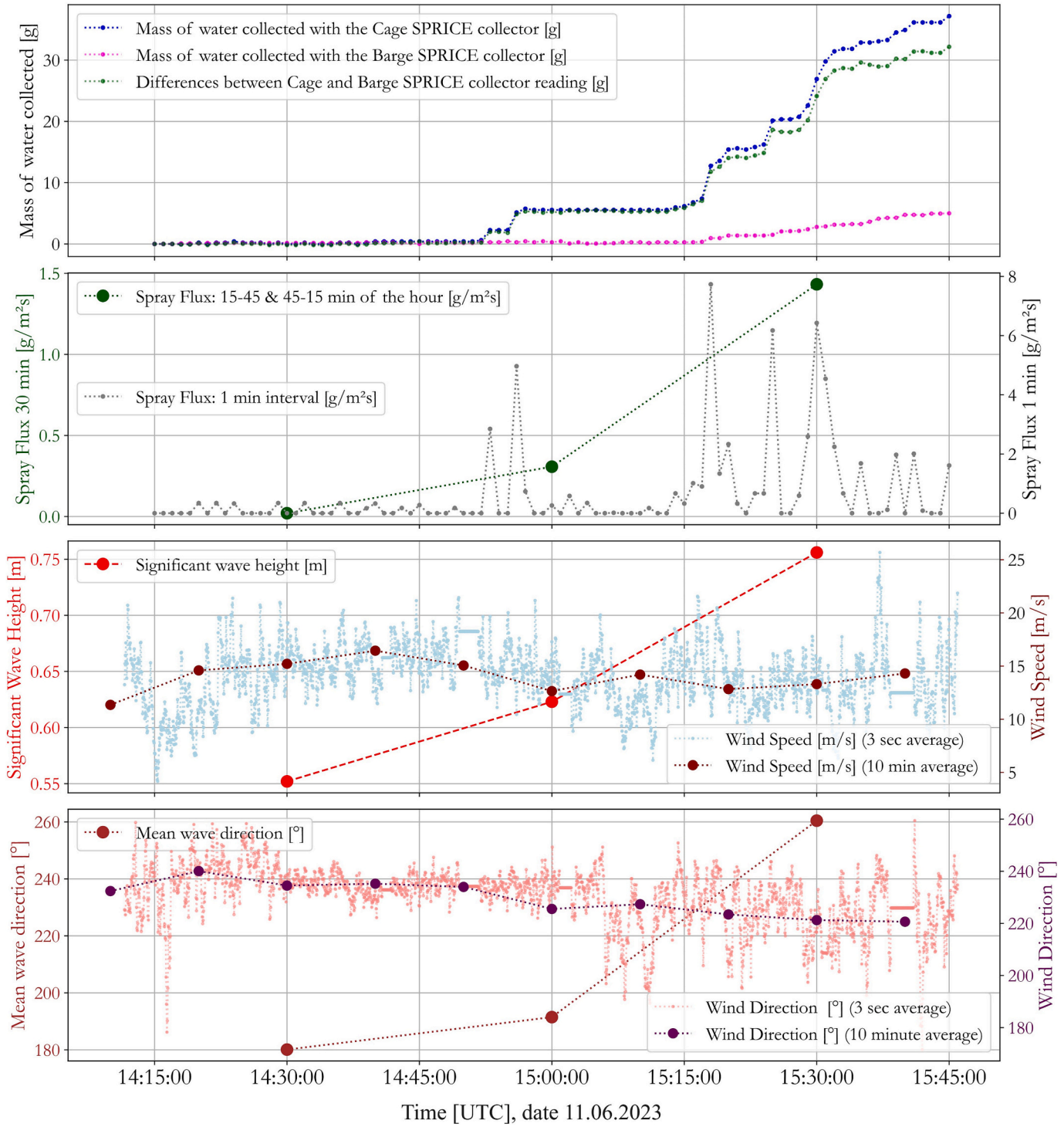

Fig. 28. (a) Time series data for mass of water collected by the SPRICE sea spray collector facing west-southwest mounted on the cage (blue data points), mass of water collected by the SPRICE collector positioned on top of the feed barge representing the rain contribution (magenta data points), and the differences between these readings representing the contribution of only spray; (b) Right Axis: Spray flux calculated for each minute, Left Axis: Spray flux calculated for the 30-min period; (c) Right Axis: 3 s average wind speed data representing the wind gust, 10 min averaged data representing the mean wind speed (data from: Thies Ultrasonic Anemometer 3-D), Left Axis: Significant wave height from wave buoy (data from: OBS-Buoy400); (d) Right Axis: 3 s average wind direction data representing the wind gust direction, 10 min averaged data representing the mean wind direction (data from: Thies Ultrasonic Anemometer 3-D), Left Axis: Mean wave direction (data from: OBS-Buoy400). (For interpretation of the references to colour in this figure legend, the reader is referred to the web version of this article.)

effective spray flux measurement when the direction of spray propagation deviates from the collector's orientation. A potential solution to this issue is to fix the collector to the cage with swivel-bearing wind vane attachment and limiting the rotation range within a predefined arc.

Another constraint arises due to the position of the collector inlet, which is situated 1.2 m above the water level and 50 cm in front of the vertical pipe of the cage structure to which it is attached. With the present configuration, the inlet position could not be altered as it accommodates the necessary clearance for the Young gauge to function (to drain the collected spray from its bottom) and allows for attaching

brackets to secure the collector. This inlet location fails to intercept the spray trajectory generated by waves of lower heights that splash through the holes in the platform of the cage (Fig. 29), resulting in missed measurement. However, the collector proves effective in capturing the spray generated when wave heights are sufficiently high (as evidenced by the data presented in Fig. 28), which results in a parabolic spray trajectory (Fig. 30) that can enter through the collector inlet. Addressing this issue may require repositioning the collector inlet further back from its current location to intercept the spray trajectory effectively, although this adjustment could be challenging due to the existing fish cage design. This limitation is specific to the current structure of the fish cages used, as the collectors need to be installed close to the waterline. However, it would not be an issue for ships and other marine structures such as rigs. In this case, the design of the collector itself is not a concern; instead, it is primarily related to its positioning.

5. Conclusions

This study introduces a novel sea spray collector, designed, and developed for measuring horizontal sea-spray flux, aimed at addressing the limitations encountered by existing instruments used in prior field expeditions. The SPRICE sea spray collector incorporates a catching-type design inspired by the cyclone separator, to effectively capture and separate sea spray droplets from the airflow while ensuring a balanced inflow and outflow to avoid pressure build-up at the inlet. Through meticulous CFD simulations, the design of the collector is refined and optimised to ensure the desired airflow performance. The collector component is fabricated using 3D printing technology, utilising Nylon filament infused with carbon fibre reinforcement for enhanced durability and corrosion resistance in marine environments. The selection of the R. M. Young automatic precipitation gauge model, 50202, for the measurement of the collected spray amount is driven by its effective performance on moving platforms such as ships and marine structures, substantiated by previous researchers' experience. The physical performance of the collector is also assessed through different experimental validations conducted during lab testing.

The design of the SPRICE collector has been adjusted to attain comparable airflow performance to the CRREL horizontal spray interceptor, as evidenced by CFD simulation results. This similarity in performance is intended to achieve an inlet efficiency similar to that of the CRREL device, which is chosen as the benchmark due to its superior airflow performance among devices used by previous researchers. Notably, the SPRICE collector outperforms the CRREL interceptor in terms of retention efficiency at higher wind speeds. Unlike the CRREL interceptor, where droplets escape through the mesh and are carried away by the airflow, resulting in decreasing efficiency with increasing wind speed, the SPRICE spray collector maintains consistently high retention efficiency. The majority of spray droplets captured by the SPRICE collector end up in the measuring gauge, with only minimal droplets escaping through the exhaust, as observed during laboratory tests.

Subsequently, the SPRICE sea spray collector is deployed on a fish farm in Northern Norway, evaluating its viability for real-world sea-spray flux data collection. Atmospheric and oceanographic data are collected simultaneously from the location to establish correlations with wind and wave parameters. The preliminary data provides valuable insights into the collector's ability, and the limitations encountered in capturing sea-spray flux under particular weather conditions. While aspects of attachment and positioning of the collector need addressing for effective spray flux data collection on fish farm cages, the design of the collector demonstrates effective functionality, in particular for collecting horizontal spray.

Overall, the SPRICE sea spray collector presents a practical solution for measuring sea-spray flux on vessels and marine structures. Its autonomous real-time measurement capability remains effective even in demanding marine weather conditions. As the study progresses and more data is gathered, a comprehensive understanding of sea-spray generation and its correlation with wave and wind parameters is anticipated. This will possibly contribute to the development of a robust sea-spray flux formulation and enhancement in marine icing estimation models.

Declaration of generative AI and AI-assisted technologies in the writing process

During the preparation of this work, the author(s) used ChatGPT in order to improve readability and language. After using this tool/service, the author(s) reviewed and edited the content as needed and take(s) full responsibility for the content of the publication.

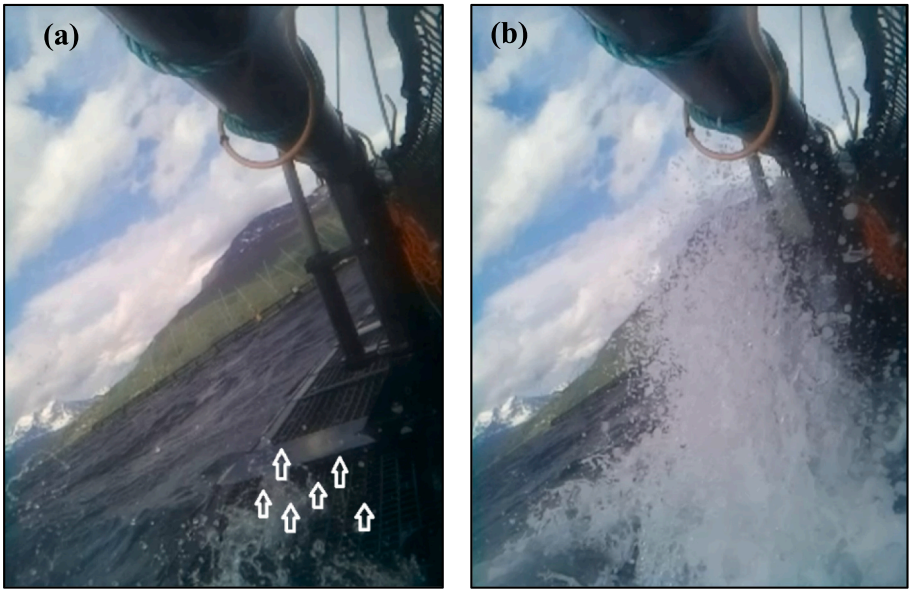

Fig. 29. (a) Spray being generated through the holes in the fish cage platform; (b) Resulting spray trajectory during lower wave heights.

Fig. 30. Illustrating the spray trajectory resulting from collisions between waves and the cage structure during higher wave heights.

CRediT authorship contribution statement

Sushmit Dhar: Conceptualization, Formal analysis, Investigation, Methodology, Writing – original draft. **Masoud Naseri:** Funding acquisition, Investigation, Methodology, Project administration, Supervision, Validation, Writing – review & editing. **Hassan Abbas Khawaja:** Conceptualization, Investigation, Methodology, Writing – review & editing. **Kåre Edvardsen:** Investigation, Supervision, Writing – review & editing. **Tiantian Zhu:** Investigation, Writing – review & editing.

Declaration of Competing Interest

The authors declare that they have no known competing financial interests or personal relationships that could have appeared to influence the work reported in this paper.

Data availability

Data will be made available on request.

Acknowledgements

We express our gratitude to the Research Council of Norway for their financial backing, provided through the "Multidisciplinary approach for spray icing modelling and decision support in the Norwegian maritime sector" (SPRICE) project, funded under the MAROFF-2 Programme [Grant Number: 320843]. We extend our appreciation to Gratanglaks AS for their generous provision of site access and resources for instrument deployment, as well as the invaluable assistance of their workers during installation and throughout the study. Special thanks also to Pål Konrad Vevang and Kristian G. Andersen for their contributions to the fabrication of the equipment.

Appendix A. CFD method

A.1. Computation domain and boundary condition

A rectangular computational domain is used to emulate the wind tunnel environment. The undisturbed wind speed was imposed parallel to the longest side (x-axis) (Fig. A.1.). The SPRICE spray collector is positioned at the centre of this domain. The x-axis runs along the longitudinal direction of the domain, the y-axis along the width, and the z-axis is along the vertical direction. The origin point of these axes is at the base of the device in the centre of their cross-section. The simulation parameters are summarised in Table A.1. This setup allows for the study of airflow and related phenomena in a controlled virtual environment resembling a wind tunnel.

Table A.1
Simulation parameters.

Model	RANS, steady-state, k-ω SST, isothermal, incompressible
Gravitational acceleration	9.81 m/s^2
Fluid Air (gas)	molecular mass 0.02896 kg/mol

(*continued on next page*)

Table A.1 (*continued*)

Model	RANS, steady-state, k-ω SST, isothermal, incompressible
Boundary conditions	wall (adiabatic, no slip)
Initial and ambient conditions	Pressure = 101,325 Pa, Temperature = 293.2 K
Free-stream wind speed along x	5, 15, 30 m/s
Domain	length $x = 3$ m, height $z = 2$ m, width $y = 2$ m

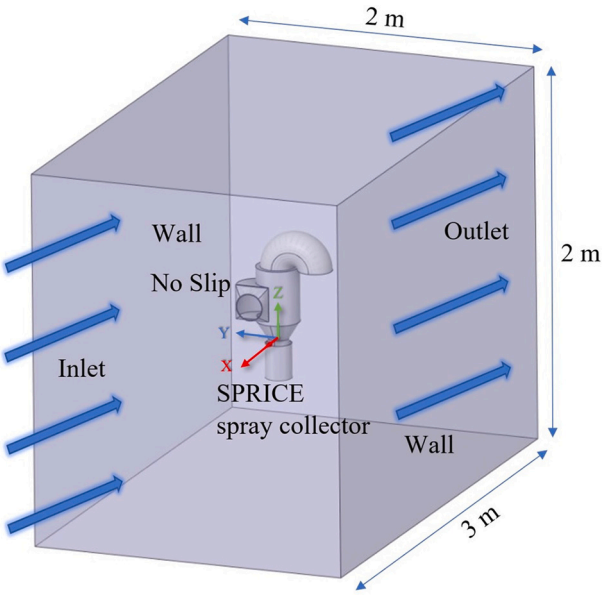

Fig. A.1. The simulated wind tunnel setup.

A.2. Discretisation

Tetrahedral elements are applied to mesh the domain used in the study. Meshing is an essential part of a CFD for rendering reliable results and needs to be refined accordingly to capture the flow details. The study includes a mesh independence test (Fig. A.2.) to assess the sensitivity of numerical results to variations in the computational mesh. It was found that employing 12,140,054 mesh elements ensured consistent results for an airflow simulation at 15 m/s, striking an optimal balance between computational time and solution accuracy for the simulation scenario. Increasing the mesh resolution further did not notably alter the air average velocity on the plane in front of the device.

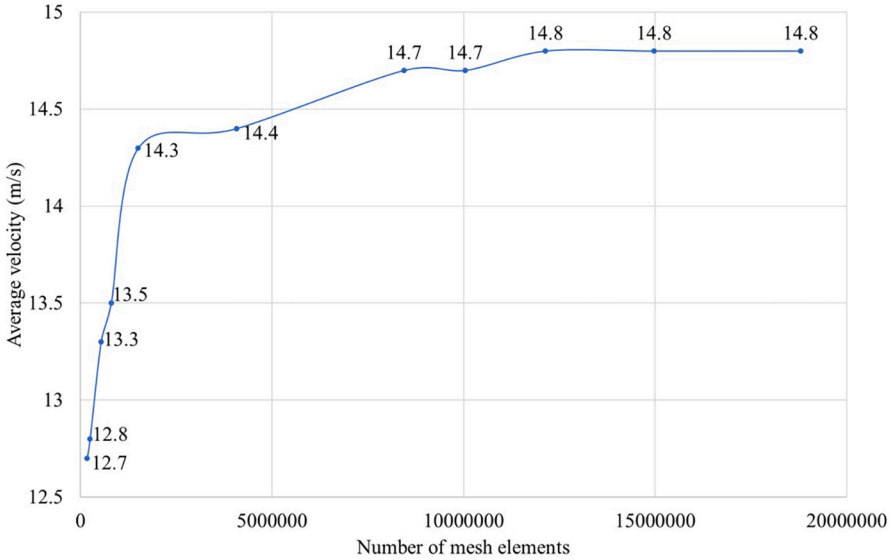

Fig. A.2. Mesh independence study at 15 m/s initial airflow velocity on plane in front of device.

References

Adolf Thies GmbH & Co KG, 2023. Thies Clima Products – Meteorology and environmental measuring technology [WWW Document]. URL. https://www.thiesclima.com/en/Products/Wind-measuring-technology-Ultrasonic-Anemometer/?art=349 (accessed 9.3.23).

AKVA Group, 2023. Plastic Pens [WWW Document]. URL. https://www.akvagroup.com/plastic-pens/. accessed 8.22.23.

Andreas, E.L., 2016. Sea spray generation at a rocky shoreline. J. Appl. Meteorol. Climatol. 55, 2037–2052. https://doi.org/10.1175/JAMC-D-15-0211.1.

Baller, H., 1983. Rig winterization to allow year-round drilling off northern Norway. Oil Gas J. 81 (31) (United States).

Barabadi, A., Garmabaki, A.H.S., Zaki, R., 2016. Designing for performability: an icing risk index for Arctic offshore. Cold Reg. Sci. Technol. 124, 77–86. https://doi.org/10.1016/j.coldregions.2015.12.013.

Barth, W., 1956. Berechnung und auslegung von zyklonabscheidern auf grund neuerer untersuchungen Brennstoff-Wärme-Kraft, Vol. 8, pp. 1–9.

Bergheim, A., 2012. Recent growth trends and challenges in the Norwegian aquaculture industry. Lat. Am. J. Aquat. Res. 40, 800–807.

Bodaghkhani, A., Dehghani, S.-R., Muzychka, Y.S., Colbourne, B., 2016. Understanding spray cloud formation by wave impact on marine objects. Cold Reg. Sci. Technol. 129, 114–136. https://doi.org/10.1016/j.coldregions.2016.06.008.

Borisenkov, Y.P., Zablockiy, G.A., Makshtas, A.P., Migulin, A.I., Panov, V.V., 1975. On the approximation of the spray-cloud dimensions. In: Arkticheskii i Antarkticheskii Nauchno-lssledovatiel' skii Institut, Trudy No. 317, Gidrometeoizdat, Leningrad, pp. 121–126 (in Russian).

Campbell Scientific, Inc., 2023a. CR350: Measurement and Control Datalogger [WWW Document]. URL. https://www.campbellsci.com/cr350 (accessed 9.3.23).

Campbell Scientific, Inc., 2023b. CR1000X: Measurement and Control Datalogger [WWW Document]. URL. https://www.campbellsci.com/cr1000x (accessed 9.3.23).

Campbell Scientific, Inc., 2023c. CR800: Measurement and Control Datalogger [WWW Document]. URL. https://www.campbellsci.com/cr800 (accessed 9.3.23).

Carstens, T., Jorgensen, T., Karterud, T., Skaret, O., 1984. The vhl sea spray icing tunnel. In: Presented at the In: Second International Workshop on Atmospheric Icing of Structures.

Cauteruccio, A., Brambilla, E., Stagnaro, M., Lanza, L.G., Rocchi, D., 2021. Experimental evidence of the wind-induced bias of precipitation gauges using particle image velocimetry and particle tracking in the wind tunnel. J. Hydrol. 600, 126690 https://doi.org/10.1016/j.jhydrol.2021.126690.

Cho, S.-R., Oh, E.-J., Kang, K.-J., 2017. A study of test methods of winterization performance for ship equipment. In: Presented at the The 27th International Ocean and Polar Engineering Conference. OnePetro.

Cole, R., Kinder, J., Ning, C.L., Yu, W., Chao, Y., 2011. "Bai-Long": a TAO-hybrid on RAMA, in: OCEANS'11 MTS/IEEE KONA. In: Presented at the OCEANS'11 MTS/IEEE KONA, pp. 1–10. https://doi.org/10.23919/OCEANS.2011.6106952.

Colli, M., Lanza, L., 2016. On the wind-induced undercatch in rainfall measurement using CFD-based simulations. In: EGU General Assembly Conference. Abstracts EPSC2016-13349.

Colli, M., Lanza, L.G., Rasmussen, R., Thériault, J.M., 2016. The Collection Efficiency of Shielded and Unshielded Precipitation Gauges. Part II: Modeling Particle Trajectories. J. Hydrometeorol. 17, 245–255. https://doi.org/10.1175/JHM-D-15-0011.1.

Dehghani, S.R., Muzychka, Y.S., Naterer, G.F., 2016a. Droplet trajectories of wave-impact sea spray on a marine vessel. Cold Reg. Sci. Technol. 127, 1–9. https://doi.org/10.1016/j.coldregions.2016.03.010.

Dehghani, S.R., Naterer, G.F., Muzychka, Y.S., 2016b. Droplet size and velocity distributions of wave-impact sea spray over a marine vessel. Cold Reg. Sci. Technol. 132, 60–67. https://doi.org/10.1016/j.coldregions.2016.09.013.

Dehghani, S.R., Naterer, G.F., Muzychka, Y.S., 2018. 3-D trajectory analysis of wave-impact sea spray over a marine vessel. Cold Reg. Sci. Technol. 146, 72–80. https://doi.org/10.1016/j.coldregions.2017.11.016.

Deshpande, S., Sæterdal, A., Sundsbø, P.-A., 2021. Sea spray icing: the physical process and review of prediction models and winterization techniques. J. Offsh. Mech. Arct. Eng. 143 https://doi.org/10.1115/1.4050892.

Desjardins, S., 2013. The fetch factor: incorporating a fetch dependency into the Overland algorithm. In: National Lab for Marine and Coastal Meteorology, Environment Canada [WWW Document]. URL. https://ocean.weather.gov/icing_rates/FetchFactor_Overland.pdf. accessed 10.10.23.

Dhar, S., Khawaja, H.A., 2021. Recognizing potential of LiDAR for comprehensive measurement of sea spray flux for improving the prediction of marine icing in cold conditions – a review. Ocean Eng. 223, 108668 https://doi.org/10.1016/j.oceaneng.2021.108668.

Dhar, S.L., Samuelsen, E.M., Naseri, M., Aarsæther, K.G., Edvardsen, K., 2022. Marine Engineering and Technology II, V05AT06A033. ASME. Presented at the Proceedings of the ASME 2022 41st International Conference on Ocean, Offshore and Arctic Engineering, Hamburg, Germany. Spray icing on ONEGA Vessel- A comparison of liquid water content expressions. https://doi.org/10.1115/OMAE2022-79919.

Dhar, S., Naseri, M., Khawaja, H.A., Samuelsen, E.M., Edvardsen, K., Barabady, J., 2023. Sea-spray measurement tools and technique employed in marine icing field expeditions: a critical literature review and assessment using CFD simulations. Cold Reg. Sci. Technol. 217 https://doi.org/10.1016/j.coldregions.2023.104029.

Dietz, P.W., 1981. Collection efficiency of cyclone separators. AICHE J. 27, 888–892. https://doi.org/10.1002/aic.690270603.

DNV, 2021. DNV-OS-A201, Winterization for Cold Climate Operations.

DNV, 2023. Rules for Classification of Ships, Part 6-Additional Class Notations, Chapter 6, Section 1-Cold Climate.

Doyle, J.D., Shapiro, M.A., 2000. A multi-scale simulation of an extreme downslope windstorm over complex topography. Meteorog. Atmos. Phys. 74, 83–101. https://doi.org/10.1007/s007030070027.

Forest, T.W., Lozowski, E.P., Gagnon, R., 2005. Estimating marine icing on offshore structures using RIGICE04. In: Proceedings of the 11th International Workshop on Atmospheric Icing of Structures, June, Montreal, Quebec, Canada.

Foy, C., Gates, E.M., Lozowski, E.P., 1987. Design, instrumentation, and performance of a refrigerated marine icing wind tunnel. In: Presented at the In: International Symposium on Cold Regions Heat Transfer, pp. 137–142.

H.IKEUCHI & Co.,Ltd., 2023. Spray Pattern, Spray Angle & Spray Distribution, Technical Information [WWW Document]. URL. https://www.kirinoikeuchi.co.jp/eng/technology/19/ (accessed 8.30.23).

Henry, N.L., 1995. Forecasting vessel icing due to freezing spray in Canadian east coastwaters. In: Part I: Model Physics. (Technical Report No. 95– 004A). Environment Canada, Newfoundland Weather Centre, Newfoundland and Labrador, Canada.

Hoffmann, A.C., Stein, L.E., 2008. Gas Cyclones and Swirl Tubes. Springer, Berlin, Heidelberg.

Hoffmann, A.C., Stein, L.E., 2010. Gas Cyclones and Swirl Tubes: Principles, Design, and Operation, 2nd ed. 2008 edition. ed. Springer.

Horjen, I., Vefsnmo, S., 1985. A kinematic and thermodynamic analysis of sea spray (in Norwegian). In: Offshore Icing – Phase II. (No. STF60 F85014). Norwegian Hydrodynamic Laboratory (NHL).

Horjen, I., Løset, S., Vefsnmo, S., 1986. Icing Hazards on Supply Vessels and Stand-by Boats. Report Number: STF60 A 86073, NHL (Now SINTEF).

IMO, 2017. International Code for Ships Operating in Polar Waters (Polar Code). International Maritime Organization (IMO), MEPC 68/21, London.

ISO, 2019. Petroleum and Natural Gas Industries — Arctic Offshore Structures, ISO 19906:2019.

Jebakumar, A.S., Abraham, J., 2016. Comparison of the structure of computed and measured particle-laden jets for a wide range of Stokes numbers. Int. J. Heat Mass Transf. 97, 779–786. https://doi.org/10.1016/j.ijheatmasstransfer.2016.02.074.

Jensen, Ø., 2006. Ice Loads – Ice Growth and Proposals for Measures (No. SFH80 A064062; ISBN: 82-14-03959-2). SINTEF.

Ji, L., Kuang, S., Yu, A., 2019. Numerical Investigation of Hydrocyclone Feed Inlet Configurations for Mitigating Particle Misplacement. Ind. Eng. Chem. Res. 58, 16823–16833. https://doi.org/10.1021/acs.iecr.9b01203.

Jones, K., Andreas, E., 2009. Sea Spray Icing of Drilling and Production Platforms (No. ERDC/CRREL TR-09-3).

Jones, K.F., Andreas, E., 2013. Winter measurements of sea spray at Mt. Desert Rock. In: Proceedings of the 15th International Workshop on Atmospheric Icing of Structures (IWAIS XV), At: St. John's, Newfoundland, Canada.

Jones, K.F., Andreas, E.L., 2014. Sea Spray and Icing in the Emerging Open Water of the Arctic Ocean (Annual report No. ADA617969). U.S. Army Corps of Engineers, Cold Regions Research and Engineering Laboratory.

Jorgensen, T.S., 1984. Sea spray measurements on the drilling rig 'Treasure Scout'. In: OTTER-Report No. STF88 F84038, NHL (now SINTEF) (In Norwegian).

Jorgensen, T.S., 1985. Sea spray measurements on the drilling rig 'Treasure Scout'. In: Tech. Rep. STF60 F 85015, NHL (now SINTEF).

Jorgensen, T.S., 1986. Offshore Icing – Phase II Final Report. Technical report, NHL (now SINTEF).

Kulyakhtin, A., 2014. Numerical Modelling and Experiments on Sea Spray Icing (Doctoral thesis).. NTNU.

Kulyakhtin, A., Tsarau, A., 2014. A time-dependent model of marine icing with application of computational fluid dynamics. Cold Reg. Sci. Technol. 104–105, 33–44. https://doi.org/10.1016/j.coldregions.2014.05.001.

Kulyakhtin, A., Kulyakhtin, S., Løset, S., 2013. Measurements of thermodynamic properties of ice created by frozen sea spray. In: Presented at the The Twenty-third International Offshore and Polar Engineering Conference. OnePetro.

Kulyakhtin, A., Kulyakhtin, S., Løset, S., 2016. The role of the ice heat conduction in the ice growth caused by periodic sea spray. Cold Reg. Sci. Technol. 127, 93–108. https://doi.org/10.1016/j.coldregions.2016.04.001.

Launiainen, J.M., Lyyra, M., Makkonen, L., 1983. A wind tunnel study of icing on marine structures. In: Presented at the POAC, Vol. 83, pp. 446–456.

LR, 2023. Rules and Regulations - Chapter 1 Rules for the Winterisation of Ships. Lloyd's Register.

Makkonen, L., 1987. Salinity and growth rate of ice formed by sea spray. Cold Reg. Sci. Technol. 14, 163–171. https://doi.org/10.1016/0165-232X(87)90032-2.

Markforged, 2023. X7 Industrial Carbon Fiber 3D Printer | Markforged [WWW Document]. URL. https://markforged.com/3d-printers/x7 (accessed 12.11.23).

Marsden, B., . Limitations of Ice Accretion on Offshore Aquaculture Facilities. URL: https://hdl.handle.net/10037/25364 (Master thesis). UiT The Arctic University of Norway, Norway.

Menter, F.R., 1994. Two-equation eddy-viscosity turbulence models for engineering applications. AIAA J. 32, 1598–1605. https://doi.org/10.2514/3.12149.

Menter, F., Kuntz, M., Langtry, R., 2003. Ten years of industrial experience with the SST turbulence model. Heat Mass Transf. 4.

Minsk, L.D., 1984. Assessment of Ice Accretion on Offshore Structures (No. 84–4). COLD REGIONS RESEARCH AND ENGINEERING LAB HANOVER NH.

Mintu, S., Molyneux, D., 2022. Ice accretion for ships and offshore structures. Part 1 – State of the art review. Ocean Eng. 258, 111501 https://doi.org/10.1016/j.oceaneng.2022.111501.

Mintu, S., Molyneux, D., Oldford, D., 2016. State-of-the-art review of research on ice accretion measurements and modelling. In: All Days. Presented at the Arctic Technology Conference, OTC. St. John's, Newfoundland and Labrador, Canada. https://doi.org/10.4043/27422-MS p. OTC-27422-MS.

Mintu, S., Molyneux, D., Colbourne, B., 2019. Multi-phase simulation of droplet trajectories of wave-impact sea spray over a vessel. In: Proceedings of the ASME 2019 38th International Conference on Ocean, Offshore and Arctic Engineering. Presented at the OMAE 2019, Glasgow, Scotland, UK. https://doi.org/10.1115/OMAE2019-95799.

Muzik, I., Kirby, A., 1992. Spray overtopping rates for Tarsiut Island: model and field study results. Can. J. Civ. Eng. 19, 469–477. https://doi.org/10.1139/l92-057.

Naseri, M., Barabady, J., 2016. On RAM performance of production facilities operating under the Barents Sea harsh environmental conditions. Int. J. Syst. Assur. Eng. Manag. 7, 273–298. https://doi.org/10.1007/s13198-016-0463-x.

Naseri, M., Samuelsen, E.M., 2019. Unprecedented vessel-icing climatology based on spray-icing modelling and reanalysis data: a risk-based decision-making input for arctic offshore industries. Atmosphere 10, 197. https://doi.org/10.3390/atmos10040197.

NexSens Technology, Inc., 2023. X2 Environmental Data Logger – NexSens [WWW Document]. URL. https://www.nexsens.com/products/data-loggers/x2-environmental-data-logger (accessed 9.3.23).

NORSOK Standard, 2017. NORSOK N-003:2017, Actions and Action Effects. Norwegian Technology Standards Institution, Oslo.

NTSB, 2020. Capsizing and Sinking of Commercial Fishing Vessel Scandies Rose (Marine accident report No. MAR-21/02). National Transportation Safety Board.

Obscape BV, 2023. OBS-Buoy400 Wave Buoy – Obscape [WWW Document]. URL. https://obscape.com/site/products-window-datalayer-window-datalayer-function-gtagdatalayer-pusharguments-gtagjs-new-date-gtagconfig-ua-171996987-1/wavebuoy/ (accessed 9.3.23).

OTT HydroMet, 2023. Compact Weather Sensors - WS600-UMB Smart Weather Sensor [WWW Document]. URL. https://www.lufft.com/products/compact-weather-sensors-293/ws600-umb-smart-weather-sensor-1832/ (accessed 9.3.23).

Overland, J.E., 1990. Prediction of vessel icing for near-freezing sea temperatures. Weather Forecast. 5, 62–77. https://doi.org/10.1175/1520-0434(1990)005<0062:POVIFN>2.0.CO;2.

Overland, J.E., Pease, C.H., Preisendorfer, R.W., Comiskey, A.L., 1986. Prediction of vessel icing. J. Appl. Meteorol. Climatol. 25, 1793–1806 doi:10.1175/1520-0450(1986)025<1793:POVI>2.0.CO;2.

Ozeki, T., Sagawa, G., 2013. Field observation of seawater spray droplets impinging on the upper deck of an icebreaker. In: Presented at the Proceedings of the 22nd International Conference on Port and Ocean Engineering under Arctic Conditions, Espoo, Finland, p. 7.

Ozeki, T., Shiga, T., Sawamura, J., Yashiro, Y., Adachi, S., Yamaguchi, H., 2016a. Development of sea spray meters and an analysis of sea spray characteristics in large vessels. In: Proceedings of the Twenty-Sixth (2016) International Ocean and Polar Engineering ConferencePresented at the International Society of Offshore and Polar Engineers (ISOPE). OnePetro, Rhodes, Greece.

Ozeki, T., Shiga, T., Sawamura, J., Yashiro, Y., Adachi, S., Yamaguchi, H., 2016b. Development of sea spray meters and an analysis of sea spray characteristics in large vessels. In: Proceedings of the Twenty-Sixth (2016) International Ocean and Polar Engineering Conference.

Ozeki, T., Toda, S., Yamaguchi, H., 2018. An investigation on the feature of seawater spray impinging on the R/V Mirai. In: Proceedings of the Twenty-Eighth (2018) International Ocean and Polar Engineering Conference, Presented at the International Society of Offshore and Polar Engineers (ISOPE), Sapporo, Japan.

Panov, V.V., 1976. Icing of ships. In: Arktlcheskii i Antarkticheskii Nauchno-lssledovatiel'skii Institut, Trudy No. 334, Gldrometeoizdat, Leningrad, 263 pp (in Russian).

Pollock, M.D., O'Donnell, G., Quinn, P., Dutton, M., Black, A., Wilkinson, M.E., Colli, M., Stagnaro, M., Lanza, L.G., Lewis, E., Kilsby, C.G., O'Connell, P.E., 2018. Quantifying and mitigating wind-induced undercatch in rainfall measurements. Water Resour. Res. 54, 3863–3875. https://doi.org/10.1029/2017WR022421.

R. M. Young Company, 2023. Precipitation Gauge | R. M. Young Company [WWW Document]. URL. https://www.youngusa.com/product/precipitation-gauge/. accessed 9.3.23.

Roebber, P., Mitten, P., 1987. Modelling and Measurement of Icing in Canadian Waters (no. Report (Canadian Climate Centre), nos. 87–15.). Atmospheric Environment Service, Canada, Ontario.

Ryerson, C.C., 1995. Superstructure spray and ice accretion on a large U.S. Coast Guard cutter. Atmos. Res. 36, 321–337. https://doi.org/10.1016/0169-8095(94)00045-F. Atmospheric icings of structures.

Ryerson, C.C., Longo, P.D., 1992. Ship Superstructure Icing Data Collection and Instrument Performance on USCGC Midgett Research Cruise (Report), this Digital Resource Was Created from Scans of the Print Resource. Cold Regions Research and Engineering Laboratory (U.S.).

Samuelsen, E.M., 2017. Prediction of Ship Icing in Arctic Waters – Observations and Modelling for Application in Operational Weather Forecasting (Doctoral Thesis). Faculty of Science and Technology Department of Engineering and Safety IVT, UiT Norges arktiske universitet, Norway.

Samuelsen, E.M., Graversen, R.G., 2019. Weather situation during observed ship-icing events off the coast of Northern Norway and the Svalbard archipelago. Weather Clim. Extrem. 24, 100200 https://doi.org/10.1016/j.wace.2019.100200.

Samuelsen, E.M., Edvardsen, K., Graversen, R.G., 2017. Modelled and observed sea-spray icing in Arctic-Norwegian waters. Cold Reg. Sci. Technol. 134, 54–81. https://doi.org/10.1016/j.coldregions.2016.11.002.

Serra, Y.L., A'Hearn, P., Freitag, H.P., McPhaden, M.J., 2001. ATLAS Self-siphoning rain gauge error estimates. J. Atmos. Ocean. Technol. 18, 1989–2002. https://doi.org/10.1175/1520-0426(2001)018<1989:ASSRGE>2.0.CO;2.

Song, C., Pei, B., Jiang, M., Wang, B., Xu, D., Chen, Y., 2016. Numerical analysis of forces exerted on particles in cyclone separators. Powder Technol. 294, 437–448. https://doi.org/10.1016/j.powtec.2016.02.052.

Stallabrass, J.R., 1980. Trawler Icing - a Compilation of Work Done at the National Research Council (no. NRC Report MD-56). Ottawa, CA.

Tabata, T., 1969. Studies on the ice accumulation on ships. III. Relation between the rate of ice accumulation and air, sea conditions. Low Temp. Sci. Ser. A 27, 339–349 (In Japanese).

Tabata, T., Iwata, S., Ono, N., 1963. Studies of ice accumulation on Ships-Part 1. Studies of ice accumulation on ships. Part 1. In: Low Temperature Science (Teion Kagaku) (No. A21). Ottawa, Canada.

Teigen, S.H., Ekeberg, O.-C., Myhre, B., Rustad, H., Petersen, S., Schrøder-Bråtane, E., Carlsen, S., 2019. Autonomous real-time sea spray measurement system for offshore structures. In: Proceedings of the International Conference on Port and Ocean Engineering under Arctic Conditions. Presented at the 25th International Conference on Port and Ocean Engineering under Arctic Conditions (POAC 2019).

Vefsnmo, S., 1985. Testing of the Numerical Icing Model Icing. (no. Tech. Rep. STF60 F85096, NHL.).

Venturi, G.B., 1797. Recherches expérimentales sur le principe de la communication latérale du mouvement dans les fluides, etc. chez Houel et Ducros.

Veron, F., 2015. Ocean spray. Annu. Rev. Fluid Mech. 47, 507–538. https://doi.org/10.1146/annurev-fluid-010814-014651.

Walsh, M.R., Morse, J.S., Knuth, K.V., Lambert, D.J., 1992. Ship Icing Instrumentation (Report), this Digital Resource Was Created from Scans of the Print Resource. Cold Regions Research and Engineering Laboratory (U.S.).

Weller, R., Bradley, E.F., Edson, J., Fairall, C., Brooks, I., Yelland, M., Pascal, R., 2008. Sensors for physical fluxes at the sea surface: energy, heat, water, salt. Ocean Sci. 4 https://doi.org/10.5194/osd-5-327-2008.

Zakrzewski, W.P., 1987. Splashing a ship with collision-generated spray. Cold Reg. Sci. Technol. 14, 65–83. https://doi.org/10.1016/0165-232X(87)90045-0.

Zakrzewski, W.P., Lozowski, E.P., 1989. Soviet marine icing data. In: Atmospheric Environment Service, Canadian Climate Centre Report. (No. 89–2). Ontario.